A vacuum double-crystal spectrometer for reference-free highly charged ions X-ray spectroscopy

P. Amaro, C.I. Szabo, S. Schlesser, Alexandre Gumberidze, Ernest G. Kessler Jr, Albert Henins, E.-O. Le Bigot, Martino Trassinelli, Jean-Michel Isac, Pascal Travers, et al.

A vacuum double-crystal spectrometer for reference-free highly charged ions X-ray spectroscopy

Pedro Amaro,[1,2,3] Csilla I. Szabo,[2] Sophie Schlesser,[2,4] Alexandre Gumberidze,[2,5,6] Ernest G. Kessler, Jr,[7] Albert Henins,[7] Eric-Olivier Le Bigot,[2] Martino Trassinelli,[8] Jean-Michel Isac,[2] Pascal Travers,[2] Mauro Guerra,[1] Jose Paulo Santos,[1] and Paul Indelicato[2,a)]

[1)] *Centro de Física Atómica, CFA, Departamento de Física, Faculdade de Ciências e Tecnologia, FCT, Universidade Nova de Lisboa, 2829-516 Caparica, Portugal*

[2)] *Laboratoire Kastler Brossel, École Normale Supérieure, CNRS, Université P. et M. Curie – Paris 6, Case 74; 4, place Jussieu, 75252 Paris CEDEX 05, France*

[3)] *Present address: Physikalisches Institut, Heidelberg University, D-69120 Heidelberg, Germany*

[4)] *Present address: KVI, Theory Group, University of Groningen, 9747 AA Groningen, The Netherlands*

[5)] *ExtreMe Matter Institute EMMI and Research Division, GSI Helmholtzzentrum für Schwerionenforschung, D-64291 Darmstadt, Germany*

[6)] *FIAS Frankfurt Institute for Advanced Studies, D-60438 Frankfurt am Main, Germany*

[7)] *National Institute of Standards and Technology NIST, 100 Bureau Drive, Gaithersburg, MD 20899, USA*

[8)] *Institut des Nanosciences de Paris, CNRS, Université P. et M. Curie – Paris 6, 4, place Jussieu, 75252 Paris CEDEX 05, France*

(Dated: May 19th, 2012)

We have built a vacuum double crystal spectrometer, which coupled to an electron-cyclotron resonance ion source, allows to measure low-energy x-ray transitions in highly-charged ions with accuracies of the order of a few parts per million. We describe in detail the instrument and its performances. Furthermore, we present a few spectra of transitions in Ar^{14+} , Ar^{15+} and Ar^{16+}. We have developed an *ab initio* simulation code that allows us to obtain accurate line profiles. It can reproduce experimental spectra with unprecedented accuracy. The quality of the profiles allows the direct determination of line width.

PACS numbers: 32.30.Rj, 31.30.J-, 12.20.Fv

I. INTRODUCTION

The measurement of x-ray transition energies of highly-charged ions (HCI) is one of the main methods to test bound-state Quantum Electrodynamics (BSQED) effects in strong fields. Highly-charged ions can be created, e.g., using high-energy accelerators, Electron Beam Ion Traps (EBIT), or Electron-Cyclotron Resonance Ion sources (ECRIS). Transitions between excited states and the $n = 1$ ground state in few-electron atoms or ions have been measured in a number of elements ranging from hydrogen to uranium. For medium atomic number elements, relevant to x-ray reflection Bragg spectrometry (transition energies in the 2 keV to 15 keV range), accuracies in the few tens of parts per million range have been obtained. Beam-foil spectroscopy has been employed to provide measurements in hydrogenlike and heliumlike ions like phosphorus, sulfur, argon[1] (80 ppm), iron[2,3] (90 ppm)[4] (25 ppm), germanium[5] and krypton.[6,7] The main limitation to obtain high accuracy in Beam-foil spectrometry is due to the Doppler effect. Correcting for the Doppler shift requires precise determination of the ions speed and angle of observation of the x rays emitted in flight. To get rid of this uncertainty, argon was also studied by x-ray spectrometry of recoil ions with an accuracy of 5 ppm[8,9] relative to an x-ray standard. The uncertainty then was due to the presence of satellite lines associated to electron capture in the target gas. An other method to reduce the Doppler effect was to decelerate the beam after stripping it at high energy by capturing electrons from a gas cell, in the so called "accel-decel" method. Hydrogenlike nickel was studied by this method[10] with an accuracy of 13 ppm.

More recently, devices like Electron Beam Ion Traps (EBIT), which create ions at low-energy, thus reducing considerably the Doppler effect have been used in a number of experiments. Transition energies have been measured in hydrogenlike chlorine[11], and heliumlike argon[11] and vanadium[12]. In Ref. 11, the hydrogenlike chlorine Lyman α lines are measured without the use of x-ray reference lines, with an accuracy of 10 ppm. The accuracy was later improved to 1.5 ppm without external reference.[13] This work uses a single Bragg crystal coupled to a CCD camera, which can be positioned very accurately with a laser beam reflected by the same crystal as the x rays. The reason to avoid the use of x-ray reference lines is the following. Present days x-ray standards, as can be found in 14, even though they are known with accuracies in the ppm range, are based on neutral elements with a K hole created by electron bombardment or photoionization. The shape and peak position of those lines depend on many factors like the excitation energy (see., e.g., Refs. 15–17), the chemical composition and the surface contamination of the sample. Physical effects like shake-off, Auger and Coster-Kronig effects lead to multivacancies, that distort and broaden the line shape.

[a)] Electronic mail: paul.indelicato@lkb.ens.fr

Examples of the complex structure of Kα lines in transition elements can be found, e.g., in Refs. 18–20. It is thus very difficult to use these standard lines with their quoted accuracy. Therefore, It was recently proposed to use either exotic atoms[21] or highly charged ions[22] to provide reliable, reproducible, narrow, x-ray standard lines.

The first observation of strong x-ray lines of highly charged argon ions (up to He-like) in an ECRIS was made in 2000.[23] This experiment allowed to describe the mechanism at work on the production of the different lines in the plasma.[24,25] Since then, several experiments have been performed at the Paul Scherrer Institute (PSI), using a spherically curved crystal spectrometer and an ECRIS,[26–30] leading to improved understanding of the ECRIS plasmas for Sulfur, Chlorine and Argon.[31–34] Such lines can be used, e.g., to characterize x-ray spectrometers response functions.[26] Yet specific techniques are required to measure their energy without the need for reference lines. The technique of Ref. 11, using a single flat crystal, is well adapted to the EBIT, which provides a very narrow ($\approx 100\,\mu$m), but rather weak x-ray source. The ECRIS plasmas have been shown to be very intense sources of x rays, but have diameters of a few cm. They are thus better adapted to spectrometers that can use an extended source. At low energies, cylindrically- or spherically-bent crystal spectrometers and double-crystal spectrometers (DCS) can be used, but only the latter can provide high-accuracy, reference-free measurements.

Precision spectroscopy with double-crystal x-ray spectrometers has a long history. The first DCS was conceived and employed independently by Compton[35], Bragg, James, and Bosanquet[36] and Wagner and Kulenkampff[37] to measure absolute integrated reflections of crystals. Davis and Stempel[38] used the DCS to study the width of the reflection curve. This experiments showed that the DCS was an instrument of high precision and high resolving power. They were followed by several others (see, e.g., Refs. 39 and 40), and were instrumental in establishing the dynamical diffraction theory of Darwin[41,42] and Prins[43]. The properties of the dispersive mode to reach high-resolution was found by Davis and Purks[44,45]. The DCS was then used to obtain the K-line widths of some elements[39,46]. A theoretical description of the instrument was provided by Schwarzschild[47]. A detailed technical description was given by Compton[48] and Williams and Allison[49]. Williams[50] introduced the vertical divergence correction in 1932, allowing for an improved accuracy for energy measurements. Bearden[51] provided an absolute measurement of copper and chromium K lines with the use of ruled gratings and calcite crystals in a DCS and deduced a value for the calcite lattice spacing,[52] leading the way to absolute x-ray wavelength measurements.[53]. Detailed description of the instrument can be found in classic textbooks.[54,55]

In a DCS, the first crystal, which is kept at a fixed angle, acts as a collimator, defining the direction and the energy of the incoming x-ray beam, which is analyzed by the second crystal. A first peak is obtained by scanning the second crystal angle when the two crystals are parallel (non-dispersive mode). Wagner and Kulenkampff[37] were the first to show the absence of dispersion in the parallel mode. The peak shape depends only on the reflection profile of the crystals and provides the response function of the instrument. A second peak is obtained when both crystals deflect the beam in the same direction (dispersive mode). The peak shape is then a convolution of the line shape and of the instrument response function. The position of the first crystal is the same in both modes. The difference in angle settings of the second crystal between the non-dispersive and the dispersive modes is directly connected to the Bragg angle. The DCS can be used in reflection (low-energy x rays), in which case the energy that is being measured depends only on the Bragg angle, on the crystals lattice spacing d, on the crystal index of refraction and on the geometry (distance between the entrance and exit slits and height and width of the slits) of the instrument. In this case the reflecting planes are parallel to the surface of the crystal. In transmission (high-energy), there is no index of refraction correction, and the reflecting planes are perpendicular to the surface. The DCS in both modes was used for many years to measure x-ray energies relative to a standard lines, as the crystal lattice spacing was not known. This changed dramatically with the obtainment of high-quality Si and Ge high-purity single crystals needed for the fabrication of transistors. Interferometric methods were then developed to do direct measurements of the lattice spacing in term of laser wavelength, with accuracies below 10^{-8}.[56–63] The DCS became then a way to do reference-free measurements of x-ray wavelengths, using well-measured and characterized crystals as transfer standards. Deslattes[64] designed a vacuum DCS intended for low-energy x rays measurements, with high-precision angular encoders and rotating tables.[64] A high-precision transmission instrument was constructed for high-energy x and γ rays, with angular interferometers able to measure angles to a fraction of milliarcseconds. This instrument allowed to resolve inconsistencies between different determination of x and γ ray wavelengths.[65,66] DCSs have been used to measure K lines of light elements like magnesium[67], copper[18] and heavy elements like tungsten[65] and from silver to uranium[68]. A complete tabulation of all available x-ray standards can be found in Ref. 14.

The purpose of this paper is twofold: we describe a vacuum DCS for low energy x rays, adapted to the use of an ECRIS plasma as x-ray source. This provides specific constraints as the ECRIS cannot be moved, contrary to an x-ray tube, to be set to the correct position for a given Bragg angle. Then we discuss the performance and properties of the system of a DCS coupled to an ECRIS and describe the *ab initio* simulation code that we develop to reproduce and analyze experimental spectra.

We describe a method to provide *absolute* measurements (without external reference) of line energies of inner-shell transitions in highly charged ions with an *ac-*

curacy unavailable until now. Reaching an accuracy of a few parts per million (ppm) in this context, can probe and test QED (Quantum ElectroDynamic) effects such as two-loop self energy corrections and provide new, more reliable x-ray standards in the few keV energy region.[21,26]

This article is organized as follows: in Sec. II we describe the technical features of the ECRIS and the DCS as well as their alignment. We also describe the measurement of the lattice spacing of the crystals that are used by the DCS. In Sec. III we give a brief review of the Monte-Carlo simulation used in this work. Furthermore, we discuss the experimental procedure in Sec. IV) and how one can assess the accuracy of measurements performed with a DCS in Sec. V. In Sec. VI we present an example of measurements and experimental tests performed with this experimental setup. The conclusions are presented in Sec. VII.

II. EXPERIMENTAL SETUP

A. ECRIS

An electron-cyclotron resonance ion source is a device built around a minimum-B structure, designed to trap hot electrons. The structure is composed of a magnetic bottle for longitudinal trapping, that can be made of coils or permanent magnets. An ion beam can be extracted along the symmetry axis of the bottle by applying high voltage. Transverse trapping is usually performed with a multlipol magnet, e.g., in our case a hexapole magnet. Microwaves are injected in a plasma chamber inside this structure, at a frequency resonant with the electrons cyclotron frequency on a constant $|\boldsymbol{B}|$ surface, which resembles an ellipsoid. The electric field of the microwaves can then accelerate electrons to very high energies. A gas or vapor is injected inside the plasma chamber and the atoms are then ionized and trapped in the space charge of the electrons, which have a density in the order of $10^{11}\,\mathrm{cm}^{-3}$. The plasma is submitted to an electric field through a *polarization electrode* which helps to optimize the ion production. A general description of an ECRIS can be found in, e.g., Ref. 69.

The Source d'Ions Multichargés de Paris (SIMPA), is a "supernanogan" ECRIS constructed by the Pantechnik Company[70]. The magnetic structure is made of permanent magnets, with field strength up to 1.3 T at contact. The microwave frequency is 14.5 GHz, produced by a 2 kW klystron. This source has been jointly operated by the Laboratoire Kastler Brossel (LKB) and the Institut des NanoSciences de Paris (INSP) since 2004. Numerous projects that use the extracted beam and the x-ray radiation of the ECRIS plasma have been started in atomic, plasma and surface physics.[71,72] SIMPA has been modified to allow for observation of the plasma though the polarization electrode. A sketch of the SIMPA ECRIS is presented in Fig. 1. The plasma in SIMPA has roughly a spherical shape, with a diameter of $\approx 3.3\,\mathrm{cm}$.

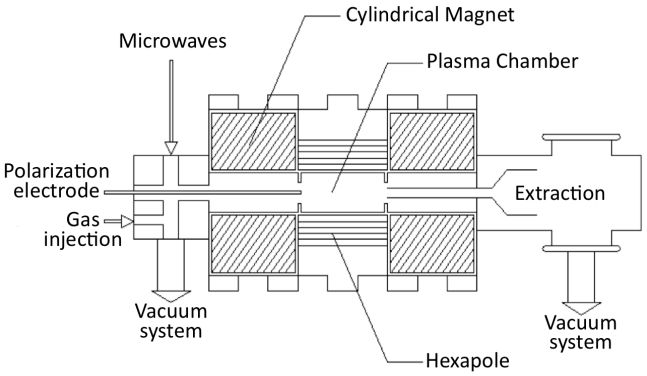

Figure 1. Principle scheme of the SIMPA ECRIS

The source has been fully characterized (electronic and ionic densities, electronic temperature, x-ray production) using x rays and extracted ion beams.[72] One consequence of the ion creation and excited level population mechanisms described in Refs. 24, 25, 31–34 is that the $1s2s\,^3S_1$ level in He-like ions is strongly populated. It is created by ionization of the Li-like ion ground state $1s^22s$. Other excited levels of He-like ions, populated by excitation of the $1s^2$ ground state of He-like ions, or by ionization and excitation mechanisms, are much less populated. This leads to the observation of a very strong $1s2s\,^3S_1 \rightarrow 1s^2\,^1S_0$ M1 transition, which is very forbidden, having a radiative width of only $10^{-7}\,\mathrm{eV}$. At the same time, the ions in the ECRIS are rather cold. They are trapped in a potential created by the space charge of the electrons, with a density of $10^{11}\,\mathrm{cm}^{-3}$, which corresponds to a potential depth lower than 1 eV. From this a Doppler broadening of $\approx 100\,\mathrm{meV}$ can be inferred. In contrast, HCI in an EBIT have have higher temperatures due to a deeper trap. The ion temperature in an EBIT was measured recently in Heidelberg and was found to be 6.9 eV[73] after evaporative cooling. This process further reduces the number of ions that can be used for spectroscopy. A detailed study of this cooling technique was recently performed in a laser spectroscopy experiment on Ar^{13+}.[74]

Observation and measurement of the $1s2s\,^3S_1 \rightarrow 1s^2\,^1S_0$ M1 transition offers a *unique* opportunity to fully characterize a spectrometer. For argon, for example, the Doppler-broadened M1 transition is roughly 8 times narrower than the width of the Kα transitions in core-excited argon (0.79 eV).[75] In the case of the DCS, for which the response function can be calculated from first principles, we can thus compare quantitatively the experimental profile and the simulated one and check the quality of the crystals.

The geometry of the SIMPA ECRIS has some influence on the positioning of the spectrometer. Figure 2 shows the distances between the plasma, the different parts and the first crystal. A picture of the installation from the source side is shown in Fig. 3. The installation of a collimator is needed to reduce the background, due, e.g., to x rays that get to the crystal without passing in-

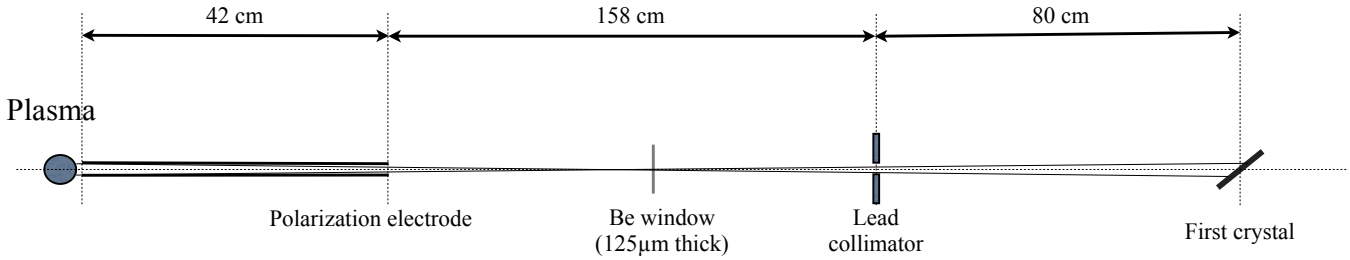

Figure 2. Geometrical arrangement of the DCS, polarization electrode, lead collimator and of the SIMPA ECRIS plasma. The inner diameter of the polarization electrode is 12 mm.

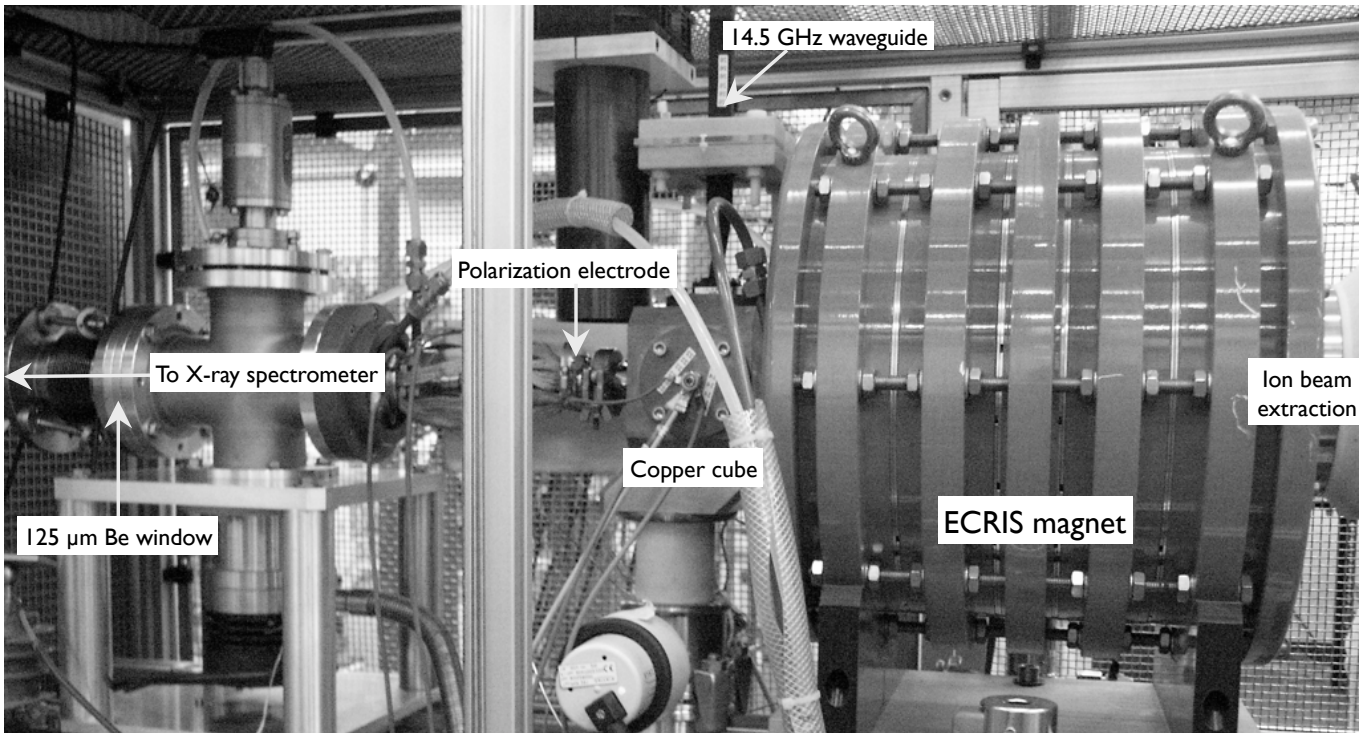

Figure 3. The SIMPA ECRIS and its connexion to the spectrometer

side the polarization electrode. Because of the collimator and polarization electrode, the x-ray beam that hits the first crystal has an angular aperture of ±6 Deg. The Be window, which isolates the vacuum of the source from the primary vacuum in the spectrometer has a transmission varying from 61% at 2991 eV to 65% at 3135 eV, an energy range that corresponds to the observation of the $1s2s^2 2p\,^1P_1 \rightarrow 1s^2 2s^2\,^1S_0$ transition in Be-like argon to the $1s2p\,^1P_1 \rightarrow 1s^2\,^1S_0$ transition in He-like argon.

All the experiments to date with this setup were performed with few-electron argon ions x rays. The microwave power injected in the source was between 250 W and 350 W. A support gas, oxygen, was injected simultaneously with argon, to provide electrons. The pressure, measured at the injection side of the ECRIS (see Fig. 3), was between 3×10^{-5} mbars and 8×10^{-5} mbars. A quadrupole mass spectrometer, positioned on the extraction side of the ECRIS allows to know the exact composition of the gas in the source, to improve the reproducibility of the ECRIS tuning.

B. Double Crystal Spectrometer

The most characteristic aspect of the DCS at SIMPA, compared to other double crystal instruments, such as the one located at NIST (National Institute of Standard and Technology)[64], is that both crystals axis are mounted on a single support table that rotates around the first crystal axis. In others DCS's, the crystals are fixed on a steady platform with the x-ray source having a rotation axis concentric with the first crystal axis.[64] The x-ray source can then be rotated so that the x-rays impinging on the first crystal meet the Bragg condition and are

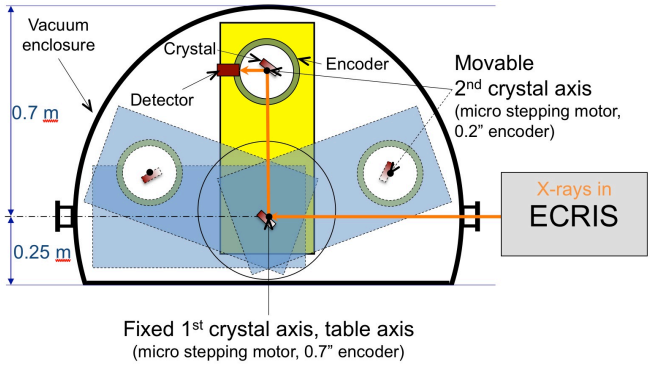

Figure 4. Scheme of the DCS.

refracted toward the second crystal.

In this experiment, the x-ray source is a massive, complicated device with several tons of fixed components (vacuum system, magnets, beam line), which makes its rotation impossible. In the design of our DCS, a heavy table supports both crystal axes, and can be rotated to adjust the instrument to an arbitrary energy range. Figure 5 shows an overall view of the spectrometer with all the major components. Both crystals supports are mounted on a single horizontal table (Fig. 5, 8), 6 cm thick and weighing ≈ 200 kg. Both supports are build so that the crystals rotate around a vertical axis (Fig. 5, 2 and 3) passing through the center of the front surface of each crystal. The spectrometer table and the rotating table supports are made of a special alloy, LK3, (0.4% C, 1.8% Cr, 1% Al, 0.25% Mo), chosen for its long-term stability. We used material that was forged at a temperature of 1100 °C and a stabilization at 900 °C was performed for 48 h. After machining, the different parts have been submitted to a stabilization annealing at 825 °C for 24 h to release strains in the material. The parts have then been finished by grinding the different surfaces to 2 μm accuracy to insure excellent parallelism of the two axes. The first crystal support weighs 63 kg and the second one 80 kg.

The spectrometer table is mounted on a heavy-duty indexing table (Fig. 5, 9), able to withstand the weight of the spectrometer assembly (≈ 360 kg), that allows to rotate it to an arbitrary angle. The assembly rotates around the same vertical axis as the first crystal axis. The indexing table is directly fixed on the lower flange of the vacuum chamber, on a surface that has been precisely machined. Because the spectrometer table is not centered on the indexing table, it is supported by a pair of conical wheels with precision ball-bearings. The conical part of the wheels has been ground to provide excellent contact. The conical wheels roll on a metallic track (Fig. 5, 11), resting on the lower vacuum chamber flange, with a system of adjustment screws. Both the track and the cone surfaces have been hardened. The wheels position can be adjusted to compensate for the table weight. The vacuum chamber weighs more than 1000 kg. It is placed on a support table with adjustable anti-vibration feet. The whole chamber can be moved for alignment with translation stages (Fig. 5, 13) made of two flat greased metallic pieces. Four screws (Fig. 5 , 16) allow to precisely position the chamber during alignment. The support table itself (Fig. 5, 14) rests on the ground with adjustable anti-vibration feet. The chamber can be pumped down to a primary vacuum of 10^{-2} mbar that reduces the absorption of the low energy x rays (around 3 keV), while being in a range of the Paschen curve for air where the detector high-voltage (2 kV) does not spark.

The rotation of the crystals is performed with precision stepping motors powered by a three-axis micro-stepping controller Newport ESP301-3G, able to perform rotations as small as 0.017". A Huber rotation stage is used for the first crystal, a Newport RV80 for the second crystal and a Newport RV240 for the detector. The angle of the first crystal is measured with a Heidenhain ROD800 encoder with a sensitivity of 0.01". Absolute angle is known with 0.5" accuracy over a full turn. The electronic control system uses the digital signal provided by the encoder to maintain the position of the crystal to the set angle over long periods of time. When the angle drifts too far away from the set position, the system stops counting x rays until the feedback control brings the angle back to the set position. For the data analysis, we use the average first crystal angle, and the standard deviation is used to define the uncertainty. The measured value for the first axis angle standard deviation ranges between 0.014" and 0.065". These positions fluctuations have a very small contribution to the total error budget. The second crystal angle is measured to a precision of 0.2" with a Heindenhain RON905 encoder, using a Heidenhain AWE1024 controller for data processing. During data acquisition, the second crystal rotates continuously at a roughly constant speed. Fluctuations in the step size however, due to backlash in the gears and non-uniformity in the stepping motor magnetic field, lead to small variation of the time spent in each bin. The scanning range is divided into a number of bins of identical size (typically 100 bins of 5.7"). The counts are stored in a bin when the angle value measured by the encoder is contained between the minimum and maximum angle defined for the bin. The content of each bin is divided by the time spent in the bin to insure proper normalization. The time during which the first axis wander too far away from the set position, leading to a stop in x rays collection is measured and subtracted from the acquisition time for a given bin. In a typical spectrum the time spent in a bin is around 13.5 s and can fluctuate between 10 s and 17 s. A typical spectrum is recorded in 10 mn in the parallel mode and in 20 mn in the dispersive mode.

A Xe (90 %) and methane (10 %) gas filled proportional counter detector is mounted on a Newport RV 280PP rotation stage with an axis of rotation concentric with the second crystal vertical axis. The detector has a 50 μm thick Be window and has an active area of about 12×25 mm^2. The detector is operated at a high

voltage of about 2000 V with and external power supply. The detector signal is processed by an ORTEC 142PC low noise charge-sensitive preamplifier and an ORTEC 572 spectroscopy amplifier with a shaping time of 6 μs. An ORTEC window and scalar module is used to generate TTL pulses when the signal amplitude corresponds to the expected x-ray energy. These pulses are accumulated by a 6602 PC card from National Instrument. A Labview program pilots the microstepping stepping motor control unit for both axes rotation stage, and for the detector rotation stage. The same program reads the AWE 1024 controller trough a GPIB bus and the first crystal encoder with an Heidenhain IK 220 PC card. The program uses the reading from the first axis encoder to maintain the angle, while scanning the second axis angle and acquiring the counts from the 6602 card. It permanently displays a graph of the crystal positions and the spectrum recorder application window.

The temperature of the crystals is measured to 0.1 °C accuracy using a calibrated Pt100 thermistor. This thermistor is also used to regulate the temperature of the crystal. A heating element is pressed between two thin copper plates, which are applied to the back of the crystal (Fig. 8). A 100 μm-thick soft graphite foil is assuring a good thermal contact between the crystal and the Cu plate in vacuum. Water cooling is applied to the rotary stages stepping motors, in order to provide sufficient heat loss when the spectrometer is under vacuum. A feedback loop controls the power in the heating element. using a proportional-integral-derivative (PID) controller method. The maximum allowed fluctuation in the course of one measurement is 0.2 K. The temperature of both crystals is also recorded during the scans with each data point registered in the data files.

C. Alignment procedure

The DCS must be carefully aligned with respect to the SIMPA axis to optimize the spectrometer throughput and allow finding easily the lines that are to be measured. The quality of the vertical alignment is very important for reducing systematic errors. The procedure is the following. First, two carefully machined cylindrical pieces with crosshairs are installed on the flange at the exit of the source in place of the Be window (see Fig. 3) and at the end of the beam line on the other side of the source (on the alignment port of the 1.5 T dipole magnet Fig. 7, a). Both ports have been aligned with the source before. A theodolite, equipped with angular encoders of arcsecond accuracy and with an electronic tilt-meter is then installed so that it is on a straight line with respect to the crosshairs. The horizontality of the axis can be verified to a few seconds of arc using the tilt-meter. The spectrometer chamber is then equipped with crosshairs on the entrance and exit flange. The theodolite is then used to align horizontally and vertically the chamber. A lead diaphragm, slightly smaller than the detector entrance window is installed on the entrance port of the spectrometer chamber, and its alignment checked. The spectrometer table is then rotated so that both crystal supports are aligned with the source axis. An alignment laser is then set to go through the crosshairs (see Fig. 7, a to d). A high-quality mirror is installed in place of the second crystal. The axis is then rotated until the laser is reflected back onto itself. The verticality of the mirror is adjusted using a micrometric screw (Fig. 8). The crystal support rotates around an axis going through the front of the mirror, using a system of flexure hinges.[76] This enables the substitution of the mirror by a crystal without losing the vertical alignment. The accuracy of this alignment is defined with the precision with which the laser beam can be centered when reflected back onto itself (see Fig. 7, e). This is around 2 mm over a distance of 16 m, i.e., 26". The angle on the encoder of the second crystal axis is then set to 90 Degrees to provide a logical reference angle for the measurements.

Once the second crystal support is aligned, the same procedure is repeated on the first crystal support. At this point both mirrors are parallel to each oder and perpendicular to the source axis. This is called the nominal alignment position. The first crystal is then rotated to the Bragg angle value corresponding to the transition to be measured, and the spectrometer table will be rotated until the laser beam hits the center of the second mirror and is reflected back onto itself. The second crystal is then rotated to the Bragg angle so that both mirrors are parallel. The x-ray detector is then positioned on the laser beam to mark the detector position for the parallel or non-dispersive mode (see Fig. 7, f). Finally the second crystal is rotated so that it is at the correct Bragg angle for the dispersive mode and the detector is moved to the correct position to check if it is correctly centered on the laser beam and to mark its position in the non-dispersive mode.

The verticality of the various components was checked with a Wyler clino 2000 tiltmeter to a precision of a few second of arcs.

The mirrors are then replaced by the crystals, and the spectrometer is set up for x-ray measurements. The ECRIS is started, and an x-ray picture is taken in front of the first crystal to check that it is uniformly illuminated. The total uncertainty associated with the alignment procedure is 0.01 Degrees. Procedures to check this alignment are presented in Secs. V and VI.

D. Crystals preparation and measurement

In order to obtain an absolute energy measurement with the DCS, it is necessary to know the crystal lattice spacing with a good accuracy. Four silicon crystals have been manufactured at NIST for the Paris DCS, two with Miller indices (111) and two with (220). Polishing procedures that lead to optical-quality surfaces (e.g., diamond powder polishing) damage the crystal surface

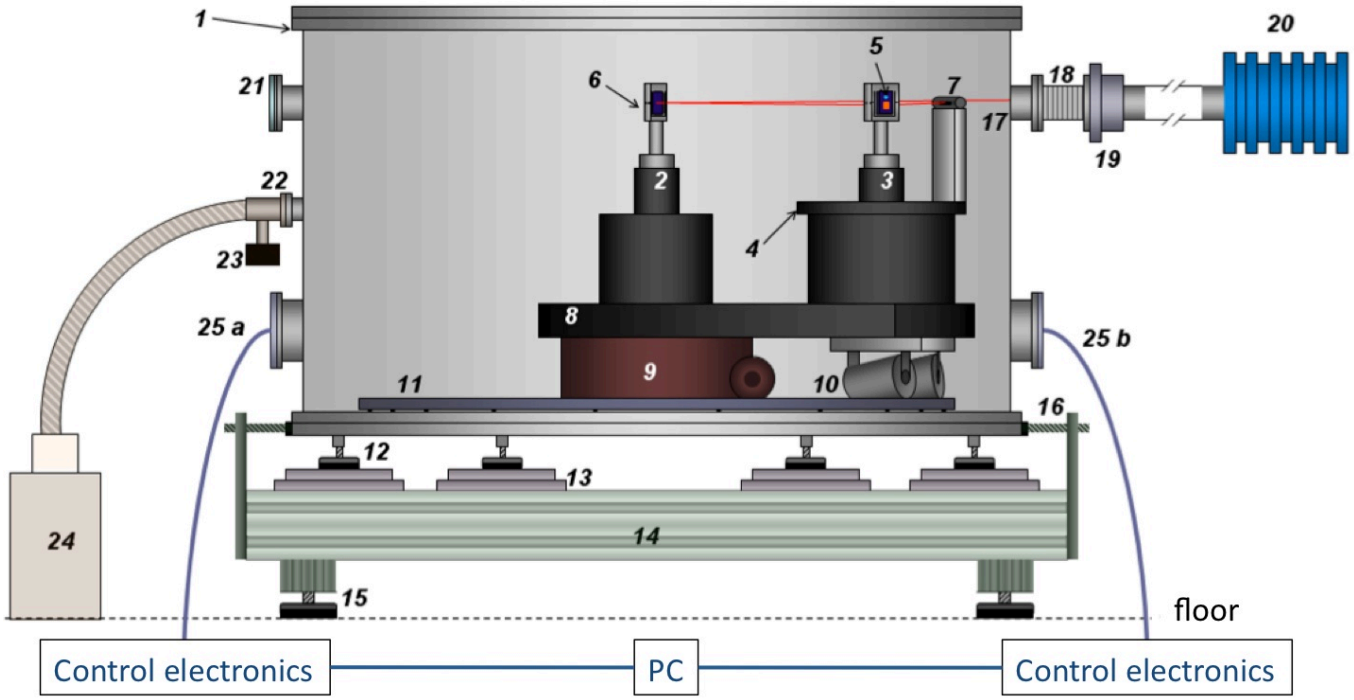

Figure 5. Spectrometer setup: 1) vacuum chamber; 2) axis #1 (first crystal support with rotation stage and angular encoder); 3) axis #2 (second crystal support, rotation stage, encoder); 4) x-ray detector rotation stage ; 5) crystal on second axis; 6) first axis crystal holder; 7) x-ray detector; 8) spectrometer table; 9) spectrometer table rotation stage; 10) conic wheels; 11) tracks for wheels; 12) vacuum chamber anti-vibration feet with vertical positioning; 13) translation stages; 14) spectrometer support table; 15) anti-vibration feet with vertical positioning; 16) positioning screws; 17) x-ray entrance; 18) bellows; 19) Be window; 20) SIMPA ECRIS; 21) optical window; 22) bellow connection to vacuum pump; 23) pressure gauge and valve; 24) primary vacuum pump; 25) a and b flanges equipped with feedthroughs for cables and cooling water

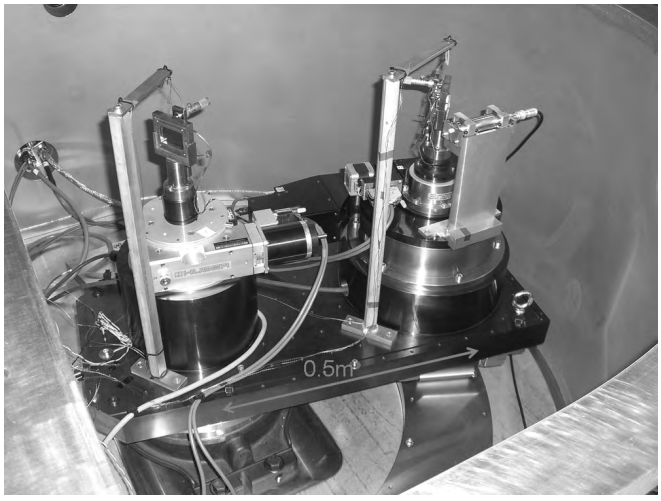

Figure 6. General view of the spectrometer.

and are not satisfactory for obtaining high-quality crystals for x-ray spectroscopy. Chemo-mechanical polishing (CMP) has been shown to lead to a somewhat broader distribution of lattice spacing values.[77] The crystals were attached to a support with wax, oriented using a crystal x-ray spectrometer and lapped, using SYTON, a colloidal silica slurry. The lapping was performed so that the cut angle (angle between crystal planes and crystal surface) is smaller than 10 arcseconds to reduce asymmetric cuts corrections to a negligible value.[55] The crystals were then etched to remove strains and surface damages and minimize lattice spacing dispersion. The crystals have thus a slightly frosted aspect, making the surface rather diffusive for laser light.

1. *Description of the measurement*

All four crystals are cut from the same boule obtained from Wacker. A small test crystal was prepared from the same boule for measurement of the lattice spacing, using the so-called "delta-d" spectrometer from NIST.[78] The physical separation between the "delta-d" diffraction crystal and the DCS diffraction crystals was kept as small as possible so that any variation in lattice spacing along the boule will have negligible influence on the determination of the lattice spacing of the DCS diffraction crystals. Although it is expected that the lattice spacings of the two samples are identical, a relative uncertainty component of 10^{-8} is included in the lattice spacing uncertainty to

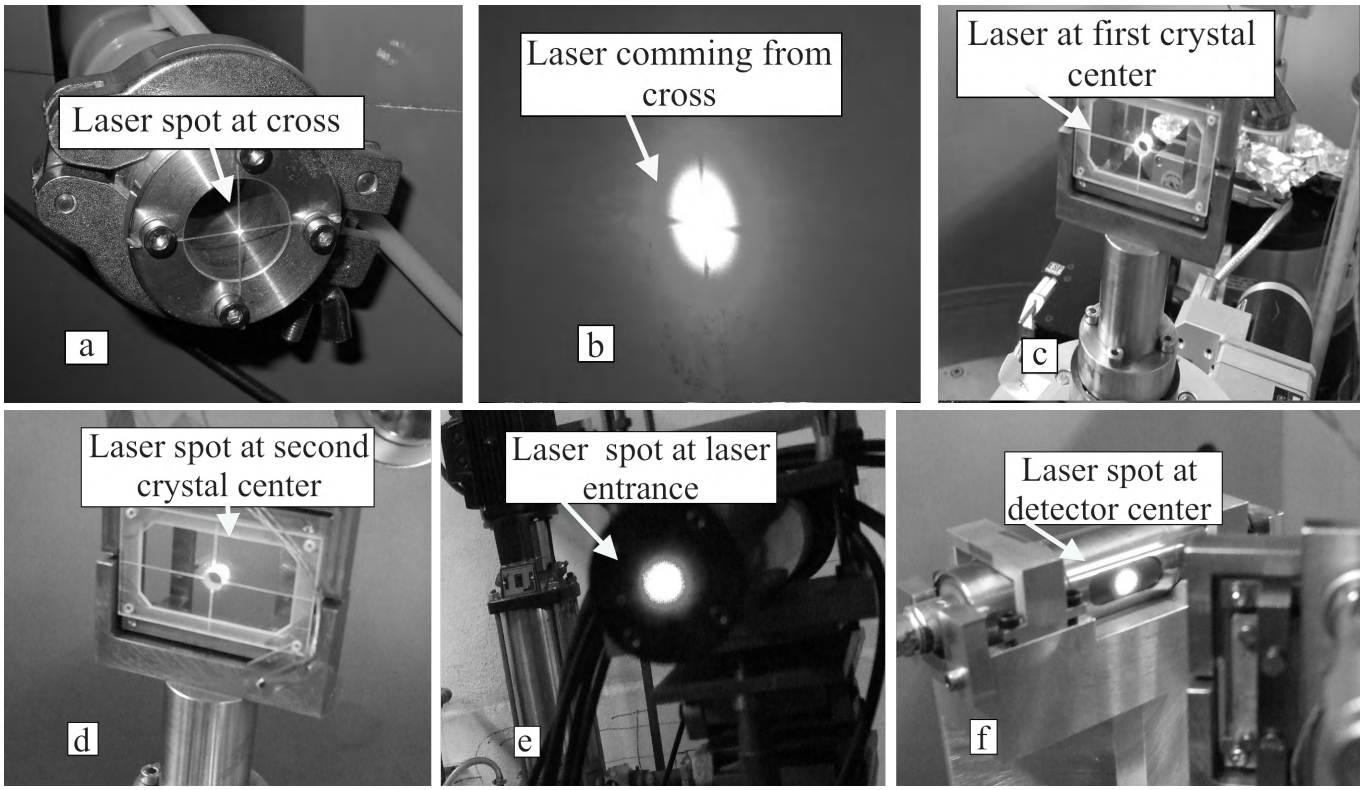

Figure 7. The laser beam is aligned with: a) cross located at back side of the ECRIS source; b) the cross located at front side of the ECRIS source (b is a picture of the out-going laser on a screen); c) the center of the first crystal; and d) the center of the second crystal. Then, a high-quality mirror is inserted in place of the second crystal. The encoder offset is set by making the laser beam goes back to the starting point e). After moving the table, the second crystal is set in the measurement position and the detector is aligned with the laser f).

account for possible sample-to-sample variations.[79] The "delta-d" crystal was etched to a lamella thickness near 0.450 mm, which was determined by fitting the "delta-d" machine spectra with theoretical diffraction profiles.

The test crystal was attached to a PZT tipper using soft wax and the crystal/PZT tipper assembly was mounted on the "delta-d" translation sled. An other sample crystal, the reference crystal, cut from the WASO04 silicon boule, was also mounted on the translation sled. The WASO04 boule is a nearly perfect single crystal silicon material that was specifically grown for the International Avogadro Project.[78–83] Nevertheless, as will be seen below, corrections for C, O, and N impurities in the WASO04 boule are taken into account in the determination of the lattice spacing of the test material.

The measurements were taken in the period from January 9 to 23, 2006. The relative difference in lattice spacing between the two crystals was measured as well as the variation in lattice spacing over the central 6 mm of the DCS crystal.

2. *Result of lattice comparison measurement*

The "delta-d" spectrometer measures the small differences in Bragg angle between two crystals, from which the lattice spacing difference of the two crystals is inferred. Silver Kα radiation is diffracted in a two-crystal transmission non-dispersive geometry and the recorded profiles are fit with theoretical dynamical diffraction profiles. A complete description of the spectrometer and the measurement procedures is available in Ref. 78.

Profiles were recorded with the second crystal position alternately being occupied by the test and reference crystal. The first crystal was rotated both clockwise and counterclockwise. Temperatures of the first crystal and of the test and reference crystals were measured at each data point and small corrections for temperature are made to the raw data before fitting. Over a 24 hour period, typical temperature changes of about 0.010 °C were noted.

The data used to obtain the lattice spacing difference between the two crystals included 150 data scans recorded over 10 days. The measured lattice spacing difference is $(d_{\rm test} - d_{\rm Ref.})/d_{\rm Ref.} = (-2.3 \pm 0.5) \times 10^{-8}$ where the uncertainty includes a statistical component (2×10^{-9}) and systematic components associated with

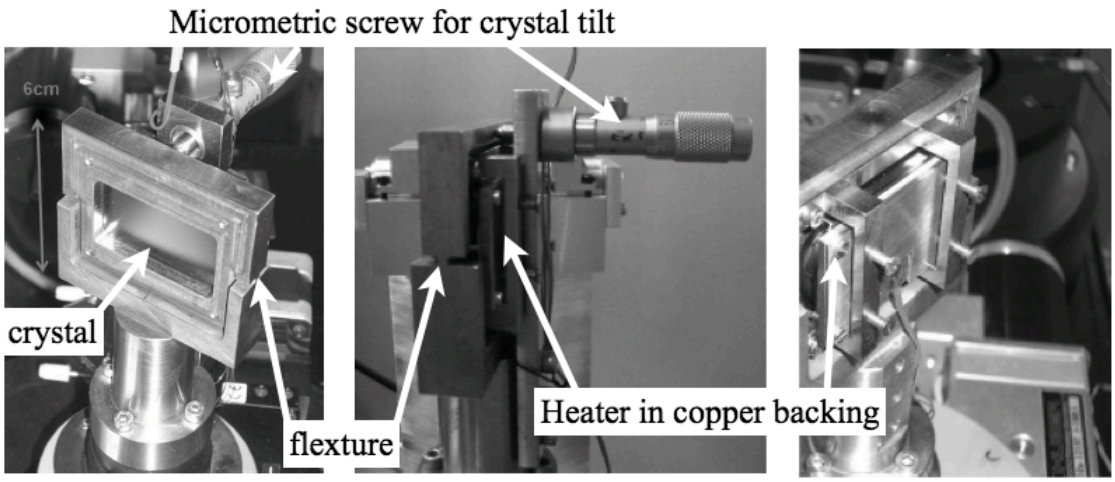

Figure 8. Details of the crystal support, with the vertical tilting system (composed of a flexture and of a micrometric screw) and the heater plate for temperature control. The copper plate ensures uniform repartition of heat on the back of the crystal. A graphite foil is positioned between the crystal and the copper plates to improve thermal contact under vacuum.

crystal temperature measurements (3×10^{-9}), crystal alignment (10^{-9}), and location of x-ray paths and crystals (3×10^{-9}).

In order to take into account variations along the Wacker and WASO04 boules, we include a relative uncertainty component of 10^{-8} and convert the measurement reported in the previous paragraph to the final result for the spectrometer crystals $(d - d_{\mathrm{WASO04}})/d_{\mathrm{WASO04}} = (-2.3 \pm 1.1) \times 10^{-8}$.

The variation of the lattice spacing along the surface of the test crystal was measured by comparing the central region with the ±3 mm regions surrounding it. The relative change in lattice spacing along this 6 mm region was measured to be 8.6×10^{-9}. This variation is consistent with the 10^{-8} relative uncertainty component that has been attributed to the lattice parameter variation along the silicon boules.

3. *Absolute lattice parameter value*

There has been several new measurement of the d_{220} lattice spacing since the publication of the 2006 CODATA recommended values of the fundamental physical constants.[81] These new measurements[61–63] leads to a large variation of the d_{220} value between the 2006 value $192.0155982(79) \times 10^{-12}$ m and the 2010 one $192.0155714(32) \times 10^{-12}$ m ($3.1\,\sigma$). This is the lattice parameter of an ideal single crystal of naturally occurring Si, free of impurities and imperfections. The numerical value for the (220) lattice spacing of Si is $\mathrm{d}_{220} = 192.0155965(70) \times 10^{-12}$ m in vacuum at 22.5 °C. Since the standard crystal in this lattice comparison measurement was taken from the WASO04 Si boule, we first adjust this value for the measured C, O, and N impurity concentrations in the WASO04 Si boule. This correction is used in the 2002 CODATA adjustment[84] where it appears as Eq. (138) on page 33. The impurity correction is shown in Table I. In the present experiment, we use the crystals in vacuum, so no pressure correction is necessary. If the crystals were to be used in a laboratory environment, a correction should be made for the compressibility of the lattice due to the laboratory atmosphere. After applying the impurity corrections, the derived value is $\mathrm{d}_{220}^{(\mathrm{WASO04})} = 192.0155311(73) \times 10^{-12}$ m for the WASO04 crystal that was used as the standard in these measurements.

Finally, the measured lattice spacing difference between crystal material WASO04 and DCS crystal material is used to calculate the absolute lattice spacing of DCS crystals $\mathrm{d}_{220}^{(\mathrm{DCS})} = 192.0155266(76) \times 10^{-12}$ m. This is the recommended absolute lattice parameter value for the diffraction crystals. Note that the dominating uncertainty component is associated with the 2010 CODATA recommended value for the d_{220} lattice spacing. Future adjustments of the fundamental physical constants will undoubtedly provide revised values for the lattice spacing of an ideal Si crystal. The results and uncertainties are summarized in Table II.

When these crystals are used at a laboratory environement for diffraction measurements, the above lattice parameter value should be adjusted for the temperature of the crystal at the time of measurement. The expansion coefficient for natural Si is $\alpha\,(\mathrm{T}) = 2.56 \times 10^{-6}\ \mathrm{C}^{\circ\,-1}$. Adjustments for changes in the laboratory air pressure are considerably smaller and can probably be ignored.

The measured lattice spacing of the Si(220) crystal is $d_{Si(220)} = 1.920155649(44)$ Å that corresponds to a lattice spacing of the Si(111) crystal equal to $d_{Si(111)} = 3.135601045(71)$ Å.

Table I. Impurity corrections in the WASO 04 crystal.[81,84] Numbers in parenthesis are uncertainties.

Coefficients	Value (cm^3)
β_C	$-6.90(0.50) \times 10^{-24}$
β_O	$4.40(0.20) \times 10^{-24}$
β_N	$5.70(1.00) \times 10^{-24}$
Impurity concentration	
Density	Value (cm^{-3})
N_C	$2.90(0.60) \times 10^{15}$
N_O	$1.30(0.20) \times 10^{15}$
N_N	$0.70(0.10) \times 10^{15}$
Impurity correction	
$\delta d/d = \beta_C N_C + \beta_O N_O + \beta_N N_N$	$-1.03(0.46) \times 10^{-8}$
additional uncertainty	1.00×10^{-8}
Final value	$-1.03(1.10) \times 10^{-8}$

Table II. Lattice spacing value for the Si (220) crystals of the spectrometer. The Si (111) values can be deduced by multiplying with the factor $\sqrt{8/3}$. Numbers in parenthesis are uncertainties.

	Value (Å)	Relative accuracy (ppm)
Ideal natural SI crystal[85]	1.920155714(32)	0.017
WASO04 (impurities)[81,84]	−0.000000020(21)	0.011
"delta-d" measurement	−0.000000045(21)	0.011
Final value (vacuum)	1.920155649(44)	0.023
Compressibility correction	−0.000000003	
Final value p = 0.987 Atm	1.920155646(44)	0.023

III. SIMULATION OF THE DCS

We have developed a ray-tracing program to obtain theoretical line profiles for the DCS, in the dispersive and non-dispersive modes. The results of this simulation program are used to analyze the experimental data. The program is based on the Monte-Carlo method and includes all relevant geometrical components of the experiment, as shown on Fig. 2, along with the crystal reflectivity curve calculated by dynamical diffraction theory (see, e.g., Ref. 86) using XOP[87–89] and checked with X0h.[90,91] This makes the simulation code capable of taking into account multiple reflexions in the crystal and corrections to the Bragg law, such as the index of refraction corrections and energy-dependent absorption. A distribution function is assigned to each x-ray line included in the simulation, to take into account its natural width (Lorentzian functions) or Doppler broadening (Gaussian function) or both (Voigt function). The simulation is thus capable of providing a line-width analysis for our experimental spectra.

A simulated line profile is represented by the number of rays hitting the detector as a function of the second crystal angle. This curve is sometimes called the rocking curve.[40] The non-dispersive profile, represented by (n_1, $-n_2$) in Allisson's notation[39], where n_i is the order of diffraction on the ith crystal, is obtained by scanning the second crystal in the case in which both crystals are parallel, as shown in Fig. 9, a). This profile is called non-dispersive since each bin in the rocking curve has contributions from all wavelengths accepted by the first crystal and reaching the second crystal. The peak in this profiles indicates that the crystallographic planes of both crystals are parallel.

The dispersive profile noted (n_1, $+n_2$) which corresponds to the geometry represented in Fig. 9, b) provides a peak for the case of a (quasi) monochromatic incoming x-ray line. The peak profile in this case is a convolution product of the instrument response function and the natural line shape. The observed intensity in this configuration is much lower than in the (n_1, $-n_2$) configuration, as each angle corresponds to only one wavelength, within the width of the crystals reflectivity curve. Up to now we have only performed measurements in first order, so we will restrict our analysis to the (1, −1) and (1, +1) cases.

The vertical geometry of the DCS in the nominal alignment position is shown in Fig. 10 to demonstrate the vertical divergence angle ϕ and the crystal tilt angles δ_1 and δ_2 used in the simulation. A succession of three xyz (orthogonal) coordinate systems are defined that follow the central line in the simulation (see Fig. 11). Each randomly generated ray will be represented in these coordinate systems within the three different parts of the experiment. The three coordinate systems are shown for the non-dispersive case in Fig. 11. The central line, that

is the line connecting the geometrical centers of the different components of an ideally aligned spectrometer defines the x, x_a, x_b axes of the three successive coordinate systems respectively.

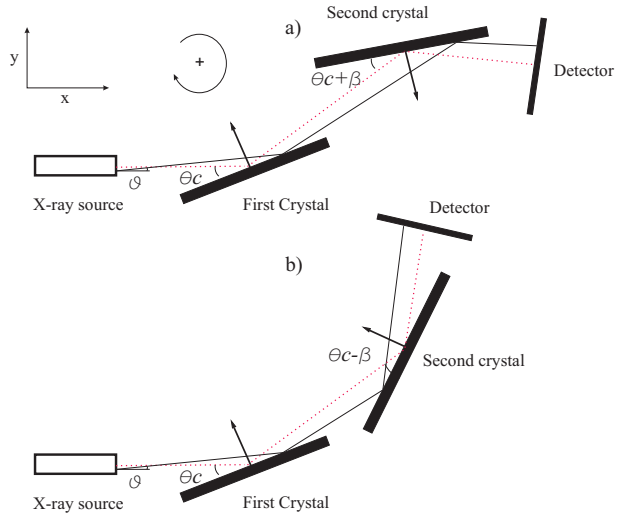

Figure 9. Geometry of the DCS in the horizontal plane. a) and b) refers to the non-dispersive and the dispersive positions respectively. The dotted line defines the central beam named "central line" in the simulation model. θ is the horizontal deviation of the x rays compared to the central line, θ_C is the central line's angle with respect to the first crystal and $\theta_C \pm \beta$ is the central line's angle with respect to the second crystal in the non-dispersive and dispersive modes respectively. The crystallographic planes of the crystals are defined by their normal vectors.

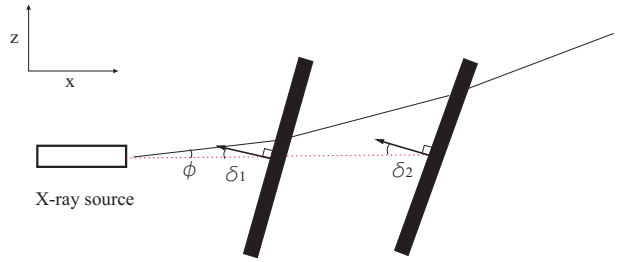

Figure 10. Geometry of the DCS in the vertical plane in the nominal alignment position (see section II. C) when the spectrometer table is placed to be parallel to the axis of the source and the crystals are rotated to be perpendicular to this same axis. This is not an actual measurement position, but serves as an example for the crystals tilts and the beam. The dotted line defines the central beam (or central line) used in the simulation model. ϕ is the vertical divergence angle of the x-ray beam at the source, δ_1 and δ_2 are the vertical tilt angles of both crystals respectively. (The tilts and vertical divergence angles are exaggerated on this figure.)

Misalignments of successive components of the experiment defined on Figs. 9 and 10 are taken into account in the simulation with respect to these three ideal xyz coordinate systems shown on Fig. 11. We define the angle

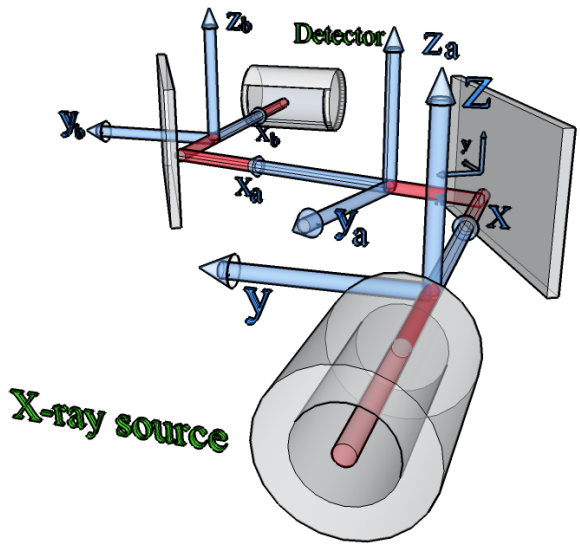

Figure 11. (Color online) Geometry of the DCS in a non-dispersive setup with the central line and the tri-orthogonal xyz axis along the central line.

θ_T as the horizontal angle between the ion source axis and the plane defined by the two crystal axes. When the experiment is properly set, we should have $\theta_T \approx 2\theta_C$ and $\theta_C \approx \theta_B$ (see Fig. 9 for the definition).

A simulated rocking curve is calculated using $\approx 10^6$ rays, each defined by generating a set of three xyz coordinates and two angles ϕ and θ with a uniform random generator, for successive values of the scanning angles β. A simulated spectrum is created by counting the number of x rays reaching the detector for a given value of β. In order to save computer time the values of ϕ and θ are constrained in the range $(\mathrm{U}[\theta_{\min}, \theta_{\max}],\ \mathrm{U}[\phi_{\min}, \phi_{\max}])$, where the angles $\theta_{\min}$, $\theta_{\max}$, $\phi_{\min}$ and $\phi_{\max}$ are given by the successive collimators between the source and the first crystal (see Fig. 2).

The ray direction is expressed by the cartesian components of the unitary vector $\hat{\boldsymbol{e}}$,

$$\begin{aligned} \hat{e}_x &= \cos(\phi)\cos(\theta)\ , \\ \hat{e}_y &= \cos(\phi)\sin(\theta)\ , \\ \hat{e}_z &= \sin(\phi) \qquad\quad . \end{aligned} \tag{1}$$

Furthermore, the initial position yz at the source-exit is defined by a fixed uniform random distribution $(\mathrm{U}[-R_c, R_c],\ \mathrm{U}[-R_c, R_c])$, where R_c is the source tube radius. If a position is generated outside the region $y^2 + z^2 < R_c^2$, it is discarded and another point is generated. This procedure was used for saving computer time since evaluation of trigonometric functions is minimized.

The position of the ray at the crystal in the plane $y'z'$, perpendicular to the source axis, which includes also the first crystal axis of rotation, is given by

$$y' = y + L\tan(\theta)\ ,$$
$$z' = z + L\tan(\phi)\ , \tag{2}$$

where L is the distance between the source and the first crystal. The position $y''z''$ on the surface of the first crystal is given by the projection of the position $y'z'$ over the surface axes

$$y'' = y'\frac{\cos(\theta)}{\cos(\theta+\frac{\pi}{2}-\theta_{\rm C})}\ ,$$
$$z'' = z'\frac{\cos(\phi)}{\cos(\phi+\delta_1)}\ . \tag{3}$$

The angle between the ray and the crystallographic plane of the first crystal is given by

$$\alpha_1 = \arcsin(-\hat{\boldsymbol{e}}\cdot\hat{\boldsymbol{n}}_1)\ , \tag{4}$$

where $\hat{\boldsymbol{e}}$ is the ray vector direction (Eq. (1)) and $\hat{\boldsymbol{n}}_1$ is a unitary vector perpendicular to the crystallographic planes of the first crystal expressed by

$$\begin{aligned}\hat{n}_{1x} &= -\cos(\delta_1)\cos(\theta_{\rm C})\ ,\\ \hat{n}_{1y} &= \ \ \cos(\delta_1)\sin(\theta_{\rm C})\ \ ,\\ \hat{n}_{1z} &= \ \ \sin(\delta_1)\qquad\quad .\end{aligned} \tag{5}$$

Therefore, the direction of the reflected ray is given by

$$\hat{\boldsymbol{e}}' = \hat{\boldsymbol{e}} - 2(\hat{\boldsymbol{e}}\cdot\hat{\boldsymbol{n}}_1)\hat{\boldsymbol{n}}_1\ . \tag{6}$$

If the ray position is within the boundaries of the crystal, a wavelength λ is generated using a Lorentzian random number generator. The normalized Lorentz function is given by

$$L(\lambda,\lambda_1,\Gamma_1) = \frac{\frac{\Gamma_1}{2\pi}}{(\lambda-\lambda_1)^2+\left(\frac{\Gamma_1}{2}\right)^2}\ , \tag{7}$$

where λ_1 is the transition wavelength and Γ_1 is the natural line width (FWHM) associated with the decay lifetime. The method used for generating the random number with a Lorentzian distribution is the inverse method.[92] The effect of the Doppler broadening is obtained by generating a wavelength λ' with a Gaussian random number generator centered at the wavelength λ

$$G(\lambda',\lambda,w) = \frac{2}{w}\sqrt{\frac{\ln(2)}{\pi}}\exp\left(-\frac{(\lambda'-\lambda)^2}{\left(\frac{w}{2\sqrt{\ln(2)}}\right)^2}\right), \tag{8}$$

where the FWHM w is given by the velocity distribution of the ions. The Gaussian random number generator is implemented using the Box-Muller method, also based on the inverse method.[92] In that way we generate a wavelength λ' corresponding to a Voigt profile (the convolution of the Lorentz and Gaussian distributions).

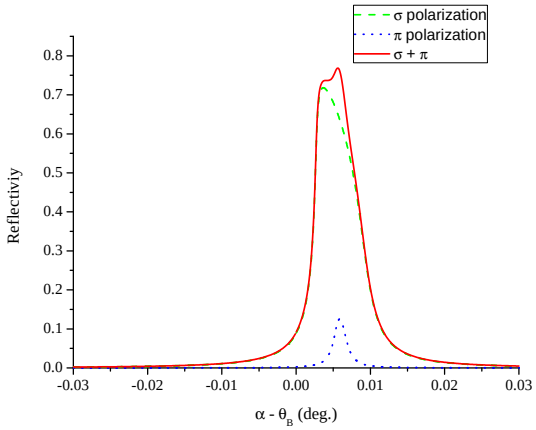

Figure 12. (Color online) Si(111) reflectivity curve for σ (green dashed) and π (blue dotted) polarizations as well as their sum (red full), evaluated with Xcrystal, a component of XOP.

The Bragg angle, $\theta_{\rm B}$, is related to the wavelength λ' by the well-know relation

$$\lambda' = 2d\sin(\theta_{\rm B})\,, \tag{9}$$

where d is the lattice spacing.

The temperature dependence of the lattice spacing is given by

$$d(T) = d_{22.5}(1+(T-22.5)\alpha(T))\,, \tag{10}$$

where the temperature is given in degrees Celcius, $\alpha(T)$ is the dilatation coefficient and $d_{22.5}$ is the lattice spacing at T = 22.5 °C. Since we are dealing with small temperature changes, we neglect the temperature dependence of $\alpha(T)$. The quantities $\alpha\,(T)$ and $d_{22.5}$ are given in Subsec. II D 3.

The reflection on the crystals is described by dynamical diffraction theory. The reflectivity curve is created using the Xcrystal component of the XOP 2.3 program[87,88] assuming an unpolarized x-ray source, and taking into account the reflections of both σ and π polarizations.Xcrystal implements the dynamical diffraction theory of Ref. 86. This program has an input option for choosing between several input files with form factors obtained from different authors (Refs. 93–98). The reflectivity curves are shown on Fig. 12 for a monochromatic line at an energy of 3104 eV. In the simulation program the reflectivity curve is interpolated using cubic splines and used as a probability distribution for the reflection of an x ray.

The reflectivity curve is evaluated at the Bragg angle corresponding to the central wavelength λ_1. The curve depends on the index of refraction and absorption coefficients, which are energy-dependent. In the

region of energy where we have performed themeasurements (3096 eV to 3139 eV) the FWHM of the reflectivity curve changes by 0.08 %/eV and the peak reflectivity by 0.1 %/eV. The same diffraction profile is used for each wavelength of an x-ray line distribution, since the variation of the diffraction profiles within the range of the peak is negligible (the typical widths of our lines are a few hundreds of meV FWHM).

The simulation program is also designed to take into account a small mosaicity of the crystal. A Gaussian distribution for the orientation of the crystal surface (θ_C) is used. When comparing experimental and simulated line profiles, we notice that this effect is very small and can be neglected. This is consistent with the fact that the crystals had a special surface treatment as described in Sec. II D. We also neglect the variation of the crystal lattice spacing as a function of position as it is measured to be small as described in Sec. II D.

Once the ray is reflected, the y_a position along the $x_a y_a z_a$ axis is given by $y_a = -y'' \sin(\theta_T - \theta_C)$. The direction vector obtained from Eq.(6) is given in this axis by multiplying it by a rotation matrix along the z axis with angle θ_T. The position vector at the second crystal in the non-dispersive or dispersive setup is obtained in the same way as for the first crystal with a translation given by Eq. (2) with L being the distance between the crystals and a projection over the surface of the second crystal. Similar to Eq. (3), the position at the second crystal crystallographic plane obtained after projection is given by

$$\begin{aligned} y_a'' &= y_a' \frac{\cos(\theta)}{\cos(\pm\theta + \theta_C \mp \beta)} \ , \\ z_a'' &= z_a' \frac{\cos(\phi)}{\cos(\phi + \delta_2)} \ , \end{aligned} \tag{11}$$

where the plus and minus signs refer to the dispersive and non-dispersive modes, respectively. As in the case of the first crystal, if the ray position is inside the second crystal, then the glancing angle between the ray direction and the second crystal surface is calculated for the reflectivity. Furthermore, similar to the first crystal evaluation part, the glancing angle is obtained from Eq. (4) with $\hat{\boldsymbol{e}}_{\boldsymbol{a}}$ defined after the first crystal reflection (Eq. (6)) and the normal vector of the second crystal $\hat{\boldsymbol{n}}_2^{\pm}$ is given by

$$\begin{aligned} \hat{n}_{2x}^{\pm} &= \mp \cos(\delta_2) \sin(\theta_T \pm \theta_C + \beta) \ , \\ \hat{n}_{2y}^{\pm} &= \pm \cos(\delta_2) \cos(\theta_T \pm \theta_C + \beta) \ , \\ \hat{n}_{2z}^{\pm} &= \sin(\delta_2) \qquad\qquad\qquad\qquad . \end{aligned} \tag{12}$$

The direction vector of the reflected ray from the second crystal is given in the $x_b y_b z_b$ coordinate system by multiplying it by a rotation matrix along the z axis with an angle $\theta_T + \theta_D^{\pm}$, where $\theta_D^{\pm}$ is the angle between the detector in the dispersive or non-dispersive modes and the axis of the source. Finally, the position of the ray at the detector entrance plane in both modes is obtained with Eq. (2) with L being the distance between the second crystal and the detector. If the ray reaches the detector, then a count is added to the simulated spectrum for the value of β.

IV. DATA ANALYSIS

In previous work, the method to deduce the energy from experiment was to fit the experimental spectrum with a Voigt profile to obtain the angle position of the peak and apply the Bragg law with index of refraction and vertical divergence corrections. The problem is that the crystal reflection curve is asymmetric (Fig. 12). In non-dispersive mode, the asymmetry disappears because the rocking curve is the convolution of the profile of Fig. 12 convolved with its mirror image. Figure 13 shows an experimental non-dispersive spectrum fitted with a Voigt profile and with a sequence of simulations, corresponding to different Gaussian broadenings of the x-ray line. It shows clearly that within the statistical uncertainty of the simulated profile the fit quality is the same as with a Voigt profile. In addition, Fig. 13 clearly demonstrates the high level of agreement between the simulation and the experimental profile. We would like to emphasize that, except for the energy used in the simulation, there is no adjustable parameter here. Moreover, since it is a non-dispersive profile, the width of the line does not change the shape as expected. In the dispersive side, the reflection curve is convolved with itself, which enhances the asymmetry. An example of a fit by a Voigt and fits by a sequence of simulated profiles is shown in Fig. 14. Again, for the profile with the width that provides the smaller χ^2, the fit quality is excellent, and the reduced χ^2 very close to 1, showing the quality of the simulation. The asymmetry of the line translates into a difference of 1.04×10^{-3} Deg between the peak positions obtained from the simulation and the Voigt fit, while it is only 1.3×10^{-4} Deg in the non-dispersive side. In the dispersive side, it corresponds to 19 times the angular encoder error. Moreover, because of the complicated line shape, the value of the angle corresponding to the peak position of the simulated profile itself is not a well defined quantity. The only well defined quantity is the energy of the line that has been used in the simulation. To avoid this problem, we used two methods. In the first one we used an analytic approximation of the profile, which allowed to have a direct relation between the energy and the peak position.[99] In a second one, we fitted both the simulated and the experimental profile with a Voigt profile. The difference in angle $\delta\theta$ and in temperature δT are used to correct the energy used in the simulation.

We write the line energy as

$$\begin{aligned} E(T,\theta) = &\frac{Cn}{2d\left(1+\alpha\left(T-T_0\right)\right)} \\ &\times \frac{1}{\sin\left(\theta+\chi\tan\theta\right)\left(1-\frac{\delta}{(\sin\theta)^2}\right)} \end{aligned} \tag{13}$$

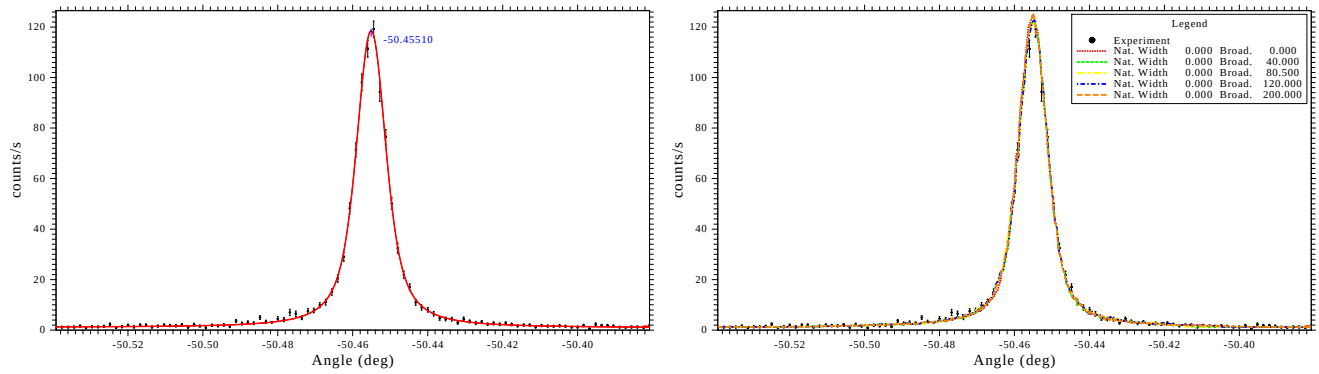

Figure 13. (Color online) Voigt profile (left) and simulated profiles with different line width (right) fitted to an experimental non-dispersive mode spectrum. The Voigt profile fit yield a $\chi^2 = 1.12$ while the simulated ones gives χ^2 ranging from 1.2 to 1.4 (the variation is mostly due to the statistic of the simulated profiles). The difference in angle is equal to 1.3×10^{-4} Degrees.

where n is the order of diffraction, δ the index of refraction, $C = hc$ is the wavelength to energy conversion facto equal to 12398.41875(31) eVÅ.[81] The coefficient χ is the vertical divergence correction

$$\chi = \frac{a^2 + b^2}{24L^2}, \tag{14}$$

where L is the distance between the slits which defines the height of the spectrometer (in our case the polarization electrode and the detector window), and L the distance between these slits. The final energy E_f is written in term of the simulation energy E_s as

$$E_f = E_s + \frac{\partial E(T,\theta)}{\partial T}\delta T + \frac{\partial E(T,\theta)}{\partial \theta}\delta\theta \tag{15}$$

The fit program uses the least-square method , with the Levenberg-Marquardt algorithm, in the implementation of Ref. 92.

The Voigt profile is a convolution product of a Lorentzian (representing the emission profile of the line) and of a Gaussian (representing an instrumental broadening), see, e.g., Ref. 100. It is written as

$$I(\theta, \theta_0, \ell, g) = I_0 \frac{K(x,y)}{K(0,y)} \tag{16}$$

with the reduced Voigt function

$$K(x,y) = \frac{y}{\pi}\int_{-\infty}^{\infty} dt \frac{e^{-t^2}}{(t-x)^2 + y^2} \tag{17}$$

$$x = \frac{2(\theta - \theta_0)\sqrt{\ln 2}}{g} \tag{18}$$

$$y = \frac{\ell}{g}\sqrt{\ln 2}, \tag{19}$$

where θ_0 is the peak position, I_0 the intensity at θ_0, ℓ the Lorentzian FWHM and g the Gaussian FWHM. The FWMH of the Voigt profile can be given to a very good approximation as:

$$w = \frac{\ell + \sqrt{\ell^2 + 4g^2}}{2}. \tag{20}$$

An exact expression was derived in Ref. 101, Eq. (21). It provides values in excellent agreement with the previous equation, but is much less convenient to use. The Voigt profile and the needed derivatives are evaluated following the method described in Ref. 100 and 102.

V. STUDY OF UNCERTAINTIES

The systematics errors in the measurement performed using the spectrometer described here can be divided into three categories. The first one consists in the uncertainties due to the alignment and to the precision of the construction of the DCS. The second one is related to uncertainties in the knowledge of diffraction profiles and on the polarization of the x rays. The third category is due to the uncertainty on the knowledge of fundamental constants or crystal properties like the lattice spacing. Uncertainties from the two first categories can be estimated with the help of the simulation program described in Sec. III. The energy deduced from simulated spectra, with various parameters varied, is evaluated following the method of Sec. IV and compared with the simulation input energy. We give in Table III the list of contributions to the final error budget for the absolute measurement of the He-like Ar $1s2s\,^3S_1 \rightarrow 1s^2\,^1S_0$ M1 transition at 3104.148 eV.[103] Most contributions to the uncertainty change very slowly with energy. The different contributions are explained below.

A. Geometrical uncertainties

The first two geometrical uncertainties are related to the alignment. The uncertainty in the verticality of the crystal diffracting planes is due to the alignment procedure described in Sec. II C and to the error in the cut angle of the crystal (Sec. II D). To this uncertainty, one has to add the one due to a possible misalignement of the DCS input collimators (Fig. 15). The total effect

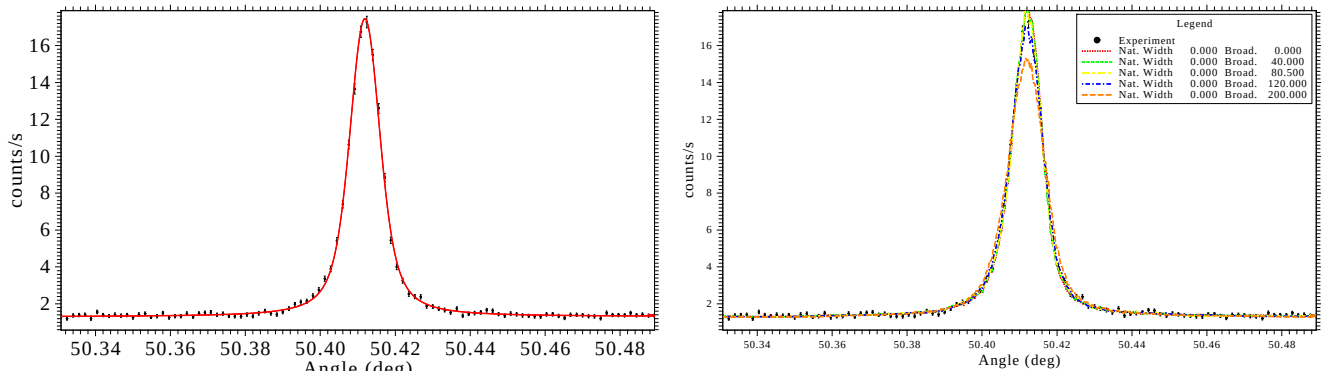

Figure 14. (Color online) Voigt profile (left) and simulated profiles with different line widths (right) fitted to an experimental dispersive mode spectrum. The Voigt profile fit yield a $\chi^2 = 1.42$ and the optimum simulated profile one (for a Gaussian broadening of 80 meV) gives a $\chi^2 = 1.26$. The difference in angle between the peak position between the two fits is equal to $1.86(7) \times 10^{-3}$ Degrees.

of these misalignments can been checked by recording x-ray spectra with absorbing masks that cover alternatively the upper and lower halves of the crystals. The comparison of the energies obtained in the two measurements gives an indication of the total uncertainty on the alignment within the statistical uncertainty of the measurement. Figure 16 shows the simulated energy difference obtained with upper and lower mask positions for several values of crystal tilts, $\delta_{1,2}$. Similarly, Fig. 17 shows the energy difference between the upper and lower mask cases for several values of vertical shifts of the lead collimator (see Fig. 15 b) that connects the source to the spectrometer.

As explained in Sec. II C, the alignment procedure provides $\delta_i \leq 0.01$ Degrees. The uncertainty related to crystal tilts was obtained from the simulation program, comparing energies from simulations using $\delta_i = 0, \pm 0.01$ Degrees. This uncertainty is in good agreement with the expressions of Bearden and Thomsen.[104]

The uncertainty related to the vertical misalignment of collimators was obtained in a similar way by running simulations with a collimator entrance shifted by ± 0.45 mm (see Fig. 15 a and b), i.e., with a vertical shift of the collimator so that $(\phi_{max} + \phi_{min})/2 = \pm 0.01$ Degrees (the total spectrometer length is 2.6 m). The relevant dimensions are given in Fig. 2). The equivalent situation for a vertical shift in the detector position is represented in Fig. 15 c). From a geometrical point of view, it is irrelevant which elements are restricting ϕ_{max} and ϕ_{min}. We thus performed a single simulation, shifting the input collimator by ± 1 mm, leading to a large overestimate of the total uncertainty.

Previous measurements with a DCS used high-power x-ray tubes to provide x-ray lines from solid targets or sometimes gas targets.[105] Here we use a plasma, the geometry and position of which are fixed by the field configuration, the microwave frequency and power, and possibly other factors like ionic and electronic temperatures, polarization electrode bias. The plasma, as fixed by the

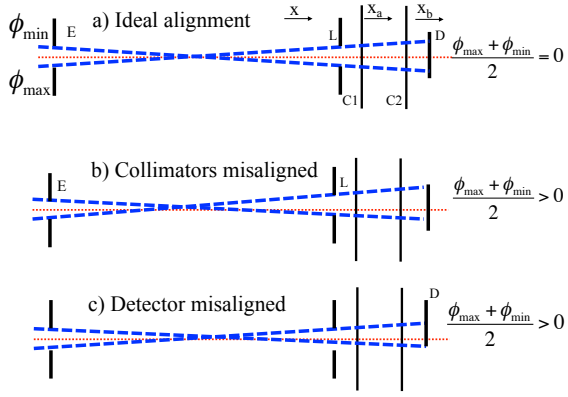

Figure 15. (Color online)Scheme of the collimator system. The points E and L refers to the entrance of the x rays and to the lead collimator respectively, as represented in Fig. 2. C1, C2 and D represents the first and second crystal and the detector, respectively. Figure a) represents an ideal alignment; Fig. b) a vertical misalignment of L compared to E; c) Fig. a vertical misalignment of the detector. The dashed lines represent rays with either maximum or minimum vertical divergence ϕ. The dotted line is the symmetry axis.

magnetic field structure, is ≈ 30 mm in diameter. Yet, x-ray imaging was performed before on ECRIS[106], which shows that the HCI position with respect to the source axis may change depending on the operation conditions. To estimate possible uncertainties due to this effect, we performed two simulations for an x-ray plasma diameter of 12 mm (diameter of the collimator) and another for a 6 mm plasma diameter. We find a difference of 1.3 meV, which we use as a largely over-estimated uncertainty in Table III.

Besides vertical and horizontal angle shifts, the case of the alignment uncertainty due to a possible vertical or horizontal translations of the crystals was also consid-

Contribution	Value (eV)
Geometrical uncertainties	
Crystal tilts ($\pm$ 0.01° for each crystal)	0.0002
Vertical misalignment of collimators (1 mm)	0.0002
X-ray source size (6 to 12 mm)	0.0013
Diffraction profile uncertainties	
Form factors	0.0020
X-ray polarization	0.0014
Instrumental limitations and uncertainties on physical constants	
Fit and extrapolation to standard temperature	0.0044
Angle encoder error (0.2 arcseconds)	0.0036
Lattice spacing error	0.0001
Index of refraction	0.0016
Coefficient of thermal expansion	0.0002
Temperature (0.5 °C)	0.0040
Energy-wavelength correction	0.0001
Total	0.0077

Table III. List of uncertainties and error contributions. The simulations were performed for a x-ray energy of 3104.148 eV, which correspond to the $1s2s\,^3S_1 \rightarrow 1s^2\,^1S_0$ transition in He-like argon. The uncertainty due to form factors was obtained by comparing simulations with different form factor values from Refs. 93–98. The x-ray polarization uncertainty is obtained by comparing a simulation done with a crystal reflection profile for a fully σ-polarized and an unpolarized beam.

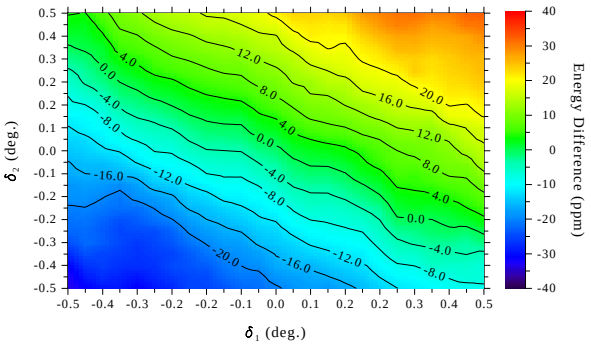

Figure 16. Plot of the energy difference (ppm) between upper and lower masks used on the second crystal for several values of crystal tilts of δ_1 and δ_2. (Color online.)

ered. No observable difference was noticed in the simulated results.

An other possible uncertainty source could be due to a small crystal curvature. Simulations performed for this effect show that the non-dispersive profile is the most sensitive to curvature. The variation of the width of the dispersive and non-dispersive profiles as a funciton of the radius of curvature are shown in Fig. 18. Changes in the dispersive side width are small, at the limit of the statistical significance. Changes in the non-dispersive side are large for radii of curvature smaller than ≈ 1000 m. The crystal curvature also induces a dependence of the non-dispersive spectra width on the first crystal angle as can be seen in Fig. 19. Finally the dependence of the line energy on the radius of curvature is plotted in Fig. 20. The figure shows that for radii of curvature larger than ≈ 5000 m the shift is much smaller than the statistical error on the fit. This effect is experimentally minimized by using thick crystals (6 mm) and nylon screws just brought to contact, to hold the crystal against the reference surface of the support as described in section II B. We are able to see experimental evidence of crystals bending when pressing them hard against their supports with strongly tightened brass screws. We were then able to observe experimentally a broadened line profiles in the non-dispersive mode, corresponding to a bending radius of ≈ 500 m and a dependence of width on the first crystal angle as reported in Fig. 19. This effect dispeared completely with the normal mode of holding the crystals, and the parallel profiles show no signs of broadening as seen in Fig. 13.

B. Diffraction profile uncertainties

The energy values obtained with a DCS in reflexion at low energy depend critically on the quality of the crystal reflectivity curve. The peak position is dependent on the index of refraction, for which few experimental determinations exists, all obtained at high energy. As described in Sec. III we use the two programs that allow to calculate reflectivity curve, XOP[87–89] and X0h[90,91] in the simulation. Moreover we use the capacity of XOP to allow choosing different form factor values.[93–98] By comparing simulations performed with the diffraction curves from the two different programs and with the different form factors, we obtain an uncertainty of 2 meV for the diffraction profile.

The index of refraction provided by XOP is 5.1005×10^{-5} for a line energy of 3104.148 eV. Henke et al. 93 provide the semi-empirical value of 5.0790×10^{-5}, and

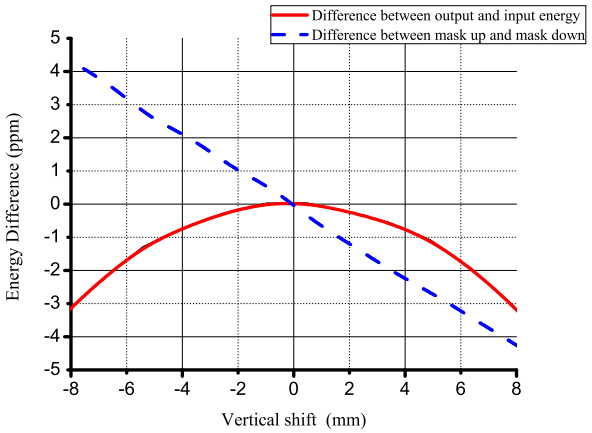

Figure 17. (Color online) Energy difference (ppm) between configurations with an upper or lower masks for several values of a vertical shift in the position of the spectrometer's collimator. The solid line is the difference between the input and output energies of the simulation. The dashed line is the difference between the simulation energy outputs for the upper and lower masks.

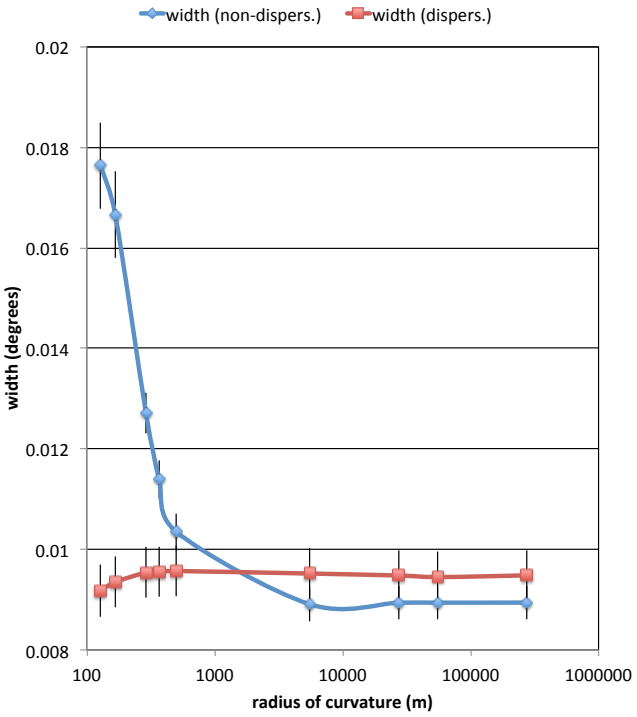

Figure 18. (Color online)Widths of the dispersive and non-dispersive profiles as a function of the crystals radius of curvature. These width are obtained by fitting simulated spectra with a Voigt profile and combining the Lorentzian and Gaussian widths using Eq. (20). Error bars are du to statistic. The dispersive and non-dispersive widths are identical for large radii of curvature as expected, within simulation statistical uncertainty.

Brennan and Cowan[107] value is 5.0825×10^{-5}. The maximum variation of the final energy using the different values of the index of refraction is 1.6 meV, which we use as an uncertainty.

The uncertainty due to unknown *polarization* of the x rays was also estimated with the use of simulations. We performed two simulations; one with a diffraction profile containing only the σ polarization and another with $\sigma + \pi$ polarization (unpolarized). From the difference a maximum uncertainty of 1.4 meV can be estimated due to the presence of any polarized light. The integrated reflectivity using only π polarization is 6 % of the the one obtained with σ polarization. This would lead to roughly 230 times fewer counts. The width of the profile obtained using only π polarized x rays is roughly 30 % smaller than the width of a profile obtained with the σ polarization. The agreement between experimental profiles widths and simulations widths performed for unpolarized x rays is excellent. This confirms within the statistical uncertainty in the experimental spectra that the x-ray beam from the ECRIS is not polarized and justify the uncertainty we quote in Table III.

We also considered other effects, like distortion of the diffraction profile due to *pendellosung*. The changes in the crystals diffraction profile at the He-like Ar M1 transition energy are presented on Fig. 21. These effects are completely washed out for crystal thicknesses above 20 μm, while our crystals have a thickness of 6 mm. The same result was obtained with both XOP and X0h.

The penetration depth of 3.1 keV x rays in Si is very small. We get 1.44 μm for σ-polarization with XOP. This correspond to an extinction length of 2.26 μm. For the π-polarization they are 7.6 μm and 12 μm respectively, but we have seen that this polarization contributes only a small fraction of the profile. We take into account the fact that each ray is reflected at a different depth in the crystal in the simulation. An exponential distribution with mean value of the *penetration depth* is used to obtain the depth where the ray is reflected. Simulations show that it would require penetration depths of a few mm to change significantly the measured energy. This effect can thus be completely neglected.

The effect of a small *mosaicity* of the crystals was also considered as a source for possible broadening of the diffraction profiles. Simulations show that non-negligible uncertainties due to this effect can only happen for values of mosaicity that produce a much larger width of simulated non-dispersive profiles than the ones observed in the experiment.

The method of alignment of the crystals for polishing give rise to an *asymmetric cut* uncertainty of ≈ 10 arcseconds (Sec. II D 1). We used XOP to estimate a possible broadening of the diffraction profile due to this and no difference was observed. We simulated the effect of an asymmetric cut of that size on the energy and found none.This uncertainty was checked experimentally by turning the crystal upside down between two measurements and by comparing the non-dispersive profiles.

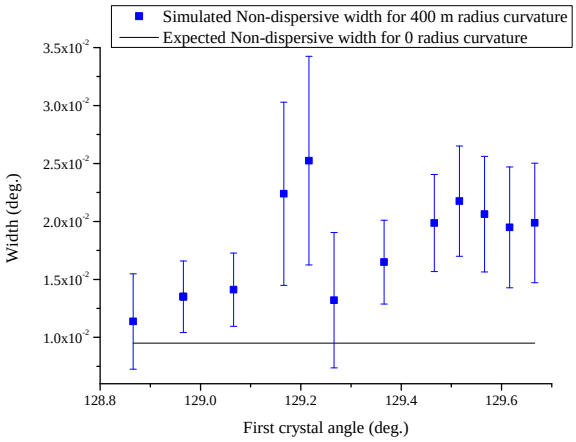

Figure 19. (Color online) Simulations performed for several values of the first crystal angle and a curvature radius of 400 m in both crystals for the He-like Ar M1 line. The simulated non-dispersive width is plotted for several values of the first crystal angle.

With the experimental statistics reachable in the current setup, we did not observe any difference in the diffraction profiles with flipped crystals. This gives us confidence on the present uncertainty due the asymmetric cut of the crystals that was guaranteed by NIST.

C. Other sources of uncertainty

As can be seen from Table III, the largest source of uncertainty comes from the statistical uncertainty of the fit, and from the extrapolation of data taken at different temperature to standard temperature (22.5 °C). To this must be added uncertainties on fundamental constants and crystal physical properties.

The main source of uncertainty lies in the difficulty of stabilizing the crystal temperatures under vacuum, with the stepping motors heating the crystal supports and the ECRIS klystron heating the room. The temperature controller is perfectly able to maintain a very stable temperature at atmospheric pressure, but not under vacuum. The use of special graphite contact sheets to improve the contact between the thermistors and the crystal could not completely fix the problem. Most of the time, it was not possible to set the temperature to below 22.7 °C. In order to alleviate this difficulty, we perform sequence of measurements at various temperatures and extrapolate to 22.5 °C. This problem leads then to two different uncertainties: one is due to the precision of the temperature measurement, which we assume to be much worse than the calibration of the thermistors. The second is due to the extrapolation procedure, and combine the statistical uncertainty of the peak position determination and the one due to the fit of a linear function to the temperature dependance of the peak position and extrapolation

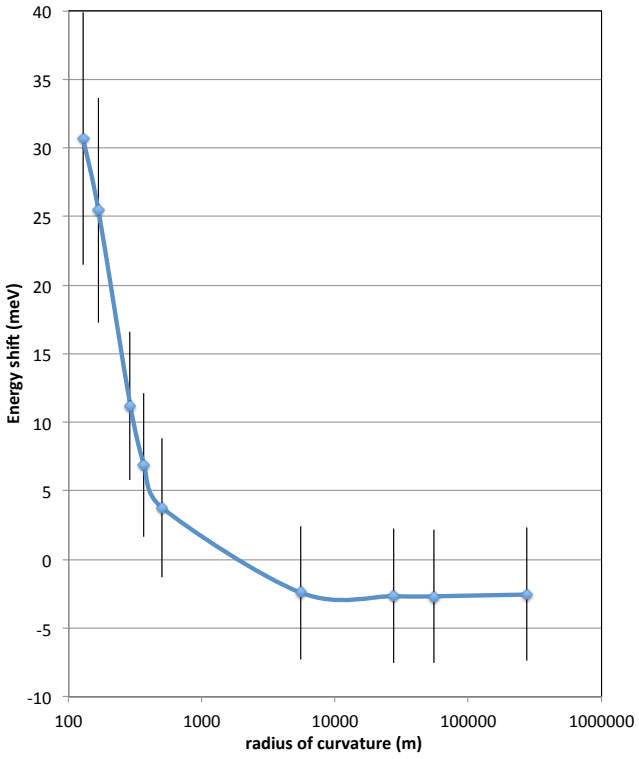

Figure 20. (Color online)Energy shift due to a curvature of the two crystals. These shifts are obtained by fitting simulated spectra with a Voigt profile. Error bars are statistical error bars.

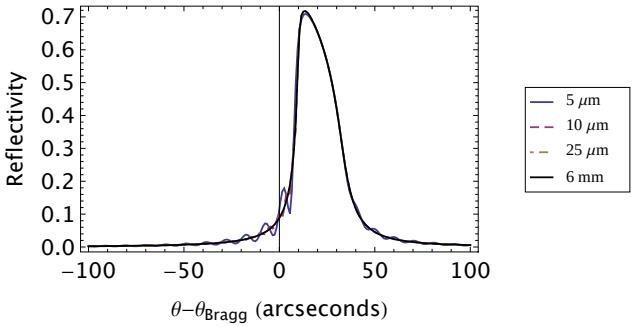

Figure 21. (Color online)Reflectivity curves for different crystal thicknesses evaluated with XOP. Only the 5 μm and the 10 μm profiles shows pendellosung oscillations.

to standard temperature. This problem will be fixed in the next version of the crystal supports, using IR sensors, which will directly measure the IR radiation from the crystals. The thermistors will no longer need to be attached to the crystals, but will be mechanically attached to the copper backing.

The next large source of uncertainty is related to the precision of the angular encoders. With a Si (1,1,1) crystal, and a Bragg angle of ≈ 39 Degrees the dispersion is such that a 0.2 arcseconds accuracy in angle measurement leads to an uncertainty of 0.0036 meV or 1.2 ppm.

This would get worse for x rays of heavier elements, giving 1.4 ppm for the M1 transition in He-like K (3.47 keV), 1.6 ppm for the M1 transition in He-like Ca (3.86 keV) and 3.1 ppm for He-like Fe (6.64 keV). Using Si (2,2,0) leads to a very small 0.4 ppm uncertainty for the M1 transition He-like potassium. One can obtain 1.7 ppm for Fe in first order and 0.2 ppm in second order. That measurement would require a very bright x-ray source. One could go beyond this limitation by doing a careful calibration of the encoder using a photoelectronic autocollimator[108] and a 24-sided optical polygon as has been done at NIST.[67,105]

The last large uncertainty in this category is related to the fact that there are no accurate measurements of the index of refraction of Si at these energies. There has been a proposition to do it by comparing directly the deflection angle in transmission and reflection, but it has not been implemented.[109] Such a measurement, if accurate could validate the theoretical or semi-empirical values[93] (which uses atomic experimental and theoretical photoabsorption cross sections) that we have used and reduce the uncertainty.

VI. RESULTS AND DISCUSSION

In Figs. 13 and 14 we present a measurement of the non-dispersive and dispersive spectra obtained with the DCS for the relativistic M1 transition $1s2s\,^3S_1 \rightarrow 1s^2\,^1S_0$ in Ar^{16+}. The data were acquired by summing individual back-and-forth 100 bins scans, lasting roughly 10 minutes in the non-dispersive case and 20 minutes in the dispersive case. The non-dispersive spectrum was acquired in 943 s and the dispersive one in 18240 s (these values are corrected for dead time, corresponding to periods when the first crystal position has drifted and is being corrected) In Fig. 22 we show a survey spectrum, in which the angular range was chosen to includes peaks corresponding to transition energies of Ar^{14+}, Ar^{15+} and Ar^{16+} ions. The tallest peak on the left side corresponds to the transition $1s^22s^22p\,^1P_1 \rightarrow 1s^22s^2\,^1S_0$ in Ar^{14+}.The the central peak is the M1 transition in Ar^{16+}. The double peak on the right corresponds to the doublet $1s2s2p\,^2P_{1/2,\,3/2} \rightarrow 1s^22s\,^2S_{1/2}$ in Ar^{15+}. A description of the mechanism leading to this spectrum can be found in Refs. 24, 25, 31–34.

The magnetic dipole (M1) transition has a natural width several orders of magnitude smaller than any line ever measured with a DCS until now. Its measured dispersive width is close to the non-dispersive peak width, which represents the intrinsic response function of the instrument. The continuous lines in Figs.13 and 14 (right) correspond to simulated profiles fitted to the measured spectra. These simulated profiles were evaluated for the case of an aligned DCS, unpolarized x rays and a diffraction profile of an ideal flat crystal, with negligible mosaicity and asymmetric cut. The simulation reproduces the non-dispersive data with a reduced $\chi^2 \approx 1.2$. This

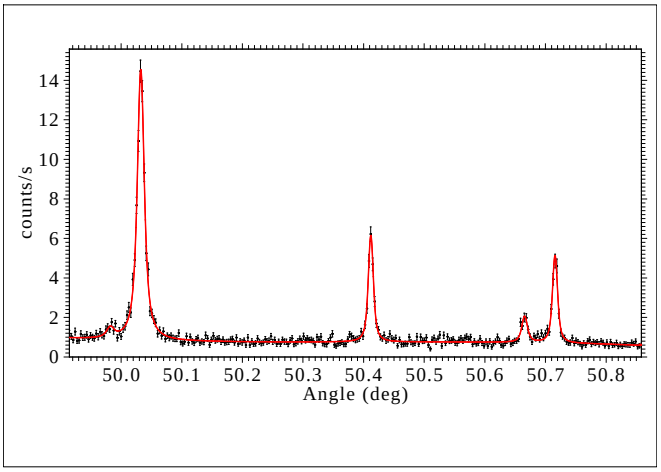

Figure 22. (color online) Experimental survey dispersive spectrum. Left peak: $1s^22s^22p\,^1P_1 \rightarrow 1s^22s^2\,^1S_0$ in Ar^{14+}, central peak: $1s2s\,^3S_1 \rightarrow 1s^2\,^1S_0$ in Ar^{16+}, left peaks: $1s2s2p\,^2P_{1/2,\,3/2} \rightarrow 1s^22s\,^2S_{1/2}$ in Ar^{15+}. The line represents a fit using a sum of Voigt profiles.

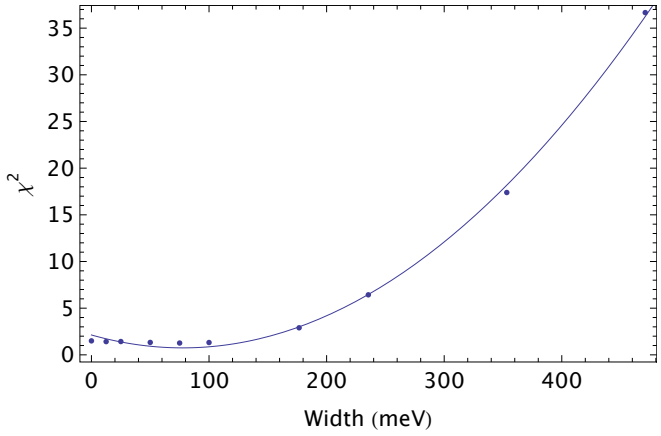

Figure 23. Variation of the χ^2 as a function of the Gaussian width introduced in the simulation to represent the Doppler broadening corresponding to the ions temperature.

precise fit of the simulated profile on the experimental spectra with no adjustable parameters except line position and intensity validates the hypothesis of perfect crystals and of an ideal alignment of the spectrometer components as made in the simulation. On the dispersive side, we fitted using simulations with various values of the Gaussian width representing the Doppler broadening due to the ion motion in the ECRIS. The dependance of the χ^2 on the width, corresponding to the spectrum of Fig. 14 is plotted on Fig. 23. The minimum corresponds to a width of 77.6(6.7) meV and to a reduced $\chi^2 = 0.75$.

In Sec. III we discussed a method for probing vertical alignment errors using crystal masking. We used this method, performing several measurements using the Be-like line (the most intense peak in Fig. 22) with a first crystal angle of 130 Degrees. In the first set of measurements, we have placed a thick brass mask on the upper

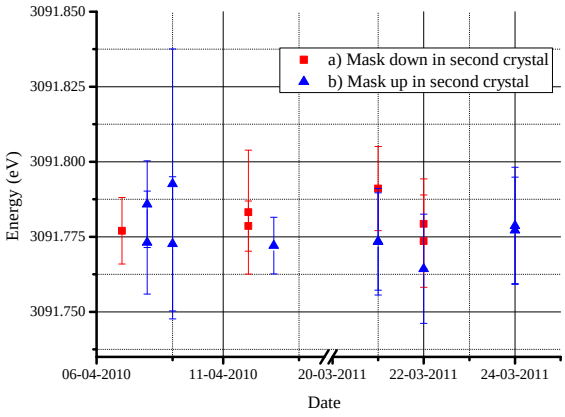

Figure 24. (color online)Plot of the energy obtained for the mask test. The red squares a) correspond to the mask placed on the lower half of the second crystal in the DCS. The blue triangles b) show measurement results for the mask placed on the upper half of the second crystal.

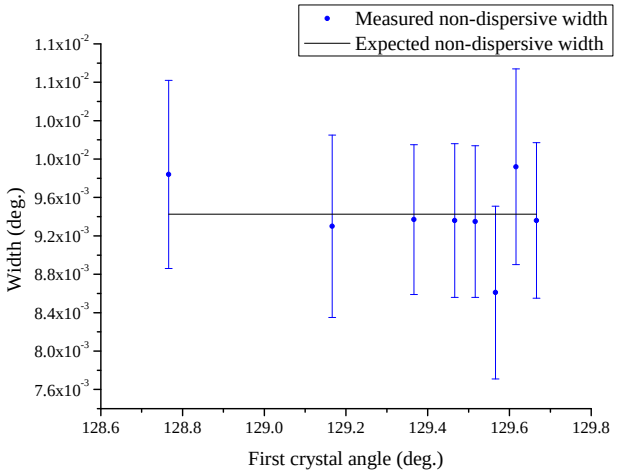

Figure 25. (Color online) Measurements of the non-dispersive width for several values of first crystal angle.

half of the second crystal. In the second set of measurements, the lower half of the second crystal was blocked with the same mask. Fig. 24 shows the line energies obtained by analyzing all the measurements performed with either mask positions. A first set of measurements was performed in April 2010, while a second set of measurements was done in March 2011. The energy obtained in the analysis using Voigt profiles for mask cowering the upper half is 3091.780 ± 0.005 eV. For a mask covering the upper half of the crystal, it is 3091.777 ± 0.005 eV, corresponding to an energy shift of 3 ± 7 meV. The uncertainty is only due to statistics. The observed shift is consistent with the one expected from the alignment uncertainty, which is 1.5 meV for 0.01 Degrees as can be seen from Fig. 17.

We also experimentally checked if a curvature in both crystals can be neglected. For that matter we performed measurements of the non-dispersive width for several values of the first crystal as is plotted in Fig. 25. Comparing Figs. 19 and 25 we notice that there is no observable dependence of the width on the first crystal angle within the statistical uncertainty.

VII. CONCLUSIONS

We provide a complete description of an experimental set-up composed of a double crystal spectrometer and of an electron-cyclotron resonance ion source, designed to measure low energy x rays from middle-Z highly-charged ions on an absolute energy scale. We experimentally demonstrated that the ECRIS plasma yield the necessary x-ray intensity to perform accurate measurements with a DCS. An *ab initio* simulation of the experimental setup (based on the spectrometer and the source geometry) is presented. The simulations describe very accurately experimental line shapes without adjustable parameters. We show by a complete sequence of measurements and simulations that we understand the systematic errors within the present statistical accuracy of the experimental spectra. The spectra presented in this work clearly show that even a relatively small, permanent magnet ECRIS provides high enough intensities for precision measurements of transitions in highly charged ions with a DCS. We also show that our understanding of the line shape is such that we can investigate the ions temperatures in the plasma. We are thus now able to obtain values of the natural line widths in ions with 2, 3 or 4 electrons, leading to a better understanding of Auger and radiative contributions to the width.

The world-wide unique combination of the DCS and the ECRIS allows to perform high-precision, reference-free measurements of x-ray transition energies in highly charged ions. These high precision measurements enable direct tests of QED and many-body effects in middle-Z elements and will provide new x-ray standards based on narrow transitions of highly charged ions.

ACKNOWLEDGMENTS

Laboratoire Kastler Brossel is "UMR n° 8552" of the ENS, CNRS and UPMC. The SIMPA ECRIS has been financed by grants from CNRS, MESR, and UPMC. The experiment is supported by grants from BNM *01 3 0002*, the ANR *ANR-06-BLAN-0223* and the Helmholtz Alliance *HA216/EMMI*.

This research was also supported in part by FCT (PEst-OE/FIS/UI0303/2011, Centro de Física Atómica), by the French-Portuguese collaboration (PESSOA Program, contract no 441.00), by the Acções Integradas Luso-Francesas (contract no F-11/09), and by the Pro-

gramme Hubert Curien PESSOA 20022VB. M. G. acknowledges the support of the FCT, under Contract SFRH/BD/38691/2007. P. A. acknowledges the support of FCT, under Contract No. SFRH/BD/37404/2007 and the German Research Foundation (DFG) within the Emmy Noether program under Contract No. TA 740 1-1. We thank J.P. Okpisz, B. Delamour, M. Boujrad, A.Vogt, and S. Souramassing for technical support, B. Manil for his help at the beginning of the spectrometer construction, and the ASUR team from INSP. We thank L. Hudson, J. Gillaspy and T. Jach for helpful discussions.

REFERENCES

[1] J. P. Briand, J. P. Mossé, P. Indelicato, P. Chevallier, D. Girard-Vernhet, A. Chétioui, M. T. Ramos, and J. P. Desclaux, Phys. Rev. A **28**, 1413 (1983).
[2] J. P. Briand, M. Tavernier, P. Indelicato, R. Marrus, and H. Gould, Phys. Rev. Lett. **50**, 832 (1983).
[3] J. P. Briand, M. Tavernier, R. Marrus, and J. P. Desclaux, Phys. Rev. A **29**, 3143 (1984).
[4] P. Indelicato, O. Gorceix, M. Tavernier, J. P. Briand, R. Marrus, and M. Prior, Z. Phys. D **2**, 149 (1986).
[5] C. T. Chantler, J. M. Laming, J. D. Silver, D. D. Dietrich, P. H. Mokler, E. C. Finch, and S. D. Rosner, Phys. Rev. A **80**, 022508 (2009).
[6] M. Tavernier, J. P. Briand, P. Indelicato, D. Liesen, and P. Richard, J. Phys. B: At. Mol. Opt. Phys. **18**, L327 (1985).
[7] P. Indelicato, M. Tavernier, J. P. Briand, and D. Liesen, Z. Phys. D **2**, 249 (1986).
[8] R. D. Deslattes, H. F. Beyer, and F. Folkmann, J. Phys. B: At. Mol. Opt. Phys. **17**, L689 (1984).
[9] H. F. Beyer, R. D. Deslattes, F. Folkmann, and R. E. LaVilla, J. Phys. B: At. Mol. Opt. Phys. **18**, 207 (1985).
[10] H. F. Beyer, P. Indelicato, K. D. Finlayson, D. Liesen, and R. D. Deslattes, Phys. Rev. A **43**, 223 (1991).
[11] H. Bruhns, J. Braun, K. Kubiček, J. R. C. Lopez-Urrutia, and J. Ullrich, Phys. Rev. Lett. **99**, 113001 (2007).
[12] C. T. Chantler, D. Paterson, L. T. Hudson, F. G. Serpa, J. D. Gillaspy, and E. Takacs, Phys. Rev. A **62**, 042501/1 (2000).
[13] K. Kubiček, J. Braun, H. Bruhns, J. R. C. Lopez-Urrutia, P. H. Mokler, and J. Ullrich, Rev. Sci. Instrum. **83**, 013102 (2012).
[14] R. Deslattes, E. Kessler, Jr, P. Indelicato, L. de Billy, E. Lindroth, and J. Anton, Rev. Mod. Phys. **75**, 35 (2003).
[15] R. D. Deslattes, P. L. Cowan, and R. E. LaVilla, AIP Conference Proceedings. no. **94**, 100 (1982).
[16] R. D. Deslattes, R. E. LaVilla, P. L. Cowan, and A. Henins, Phys. Rev. A **27**, 923 (1983).
[17] M. Deutsch, O. Gang, K. Hämäläinen, and C. C. Kao, Phys. Rev. Lett. **76**, 2424 (1996).
[18] M. Deutsch, G. Hölzer, J. Härtwig, J. Wolf, M. Fritsch, and E. Förster, Phys. Rev. A **51**, 283 (1995).
[19] G. Hölzer, M. Fritsch, M. Deutsch, J. Härtwig, and E. Förster, Phys. Rev. A **56**, 4554 (1997).
[20] M. Deutsch, E. Förster, G. Hölzer, J. Härtwig, K. Hämäläinen, C.-C. Kao, S. Huotari, and R. Diamant, Journal of Research of the National Institute of Standards and Technology **109** (2004).
[21] D. F. Anagnostopoulos, D. Gotta, P. Indelicato, and L. M. Simons, Phys. Rev. Lett. **91**, 240801 (2003).
[22] D. F. Anagnostopoulos, S. Biri, V. Boisbourdain, M. Demeter, G. Borchert, J. Egger, H. Fuhrmann, D. Gotta, A. Gruber, M. Hennebach, P. Indelicato, Y. W.Liu, N. Nelms, and L. M. Simons, Nucl. Instrum. Methods B **205**, 9 (2003).
[23] G. Douysset, H. Khodja, A. Girard, and J. P. Briand, Phys. Rev. E **61**, 3015 (2000).
[24] M. C. Martins, A. M. Costa, J. P. Santos, P. Indelicato, and F. Parente, J. Phys. B **34**, 533 (2001).
[25] A. M. Costa, M. C. Martins, F. Parente, J. P. Santos, and P. Indelicato, At. Data Nucl. Data Tables **79**, 223 (2001).
[26] D. F. Anagnostopoulos, S. Biri, D. Gotta, A. Gruber, P. Indelicato, B. Leoni, H. Fuhrmann, L. M. Simons, L. Stingelin, A. Wasser, and J. Zmeskal, Nuc. Instrum. Methods A **545**, 217 (2005).
[27] P. Indelicato, E.-O. Le Bigot, M. Trassinelli, D. Gotta, M. Hennebach, N. Nelms, C. David, and L. M. Simons, Rev. Sci. Instrum. **77**, 043107 (2006).
[28] P. Indelicato, S. Boucard, D. S. Covita, D. Gotta, A. Gruber, A. Hirtl, H. Fuhrmann, E.-O. L. Bigot, S. Schlesser, J. M. F. d. Santos, L. M. Simons, L. Stingelin, M. Trassinelli, J. Veloso, A. Wasser, and J. Zmeskal, Nucl. Instrum. Methods A **580**, 8 (2007).
[29] M. Trassinelli, S. Boucard, D. S. Covita, D. Gotta, A. Hirtl, P. Indelicato, O. L. Bigot, J. M. F. d. Santos, L. M. Simons, L. Stingelin, J. F. C. A. Veloso, A. Wasser, and J. Zmeskal, J. Phys. CS **58**, 129 (2007).
[30] E. O. Le Bigot, S. Boucard, D. S. Covita, D. Gotta, A. Gruber, A. Hirtl, H. Fuhrmann, P. Indelicato, J. M. F. d. Santos, S. Schlesser, L. M. Simons, L. Stingelin, M. Trassinelli, J. F. C. A. Veloso, A. Wasser, and J. Zmeskal, Physica Scripta , 014015 (2009).
[31] J. P. Santos, M. C. Martins, A. M. Costa, P. Indelicato, and F. Parente, Vacuum **82**, 1522 (2008).
[32] M. C. Martins, J. P. Marques, A. M. Costa, J. P. Santos, F. Parente, S. Schlesser, E.-O. Le Bigot, and P. Indelicato, Phys. Rev. A **80**, 032501 (2009).
[33] J. P. Santos, A. M. Costa, J. P. Marques, M. C. Martins, P. Indelicato, and F. Parente, Phys. Rev. A **82**, 962516 (2010).
[34] J. P. Santos, M. C. Martins, A. M. Costa, J. P. Marques, P. Indelicato, and F. Parente, Physica Scripta **2011**, 014005 (2011).
[35] A. H. Compton, in *Minutes of the Washington Meeting*, Vol. 10 (1917) p. 95.
[36] W. L. Bragg, R. W. James, and C. H. Bosanquet, Philosophical Magazine Series 6 **41**, 309 (1921).
[37] E. Wagner and H. Kulenkampff, Ann. der Phys. **373**, 369 (1922).
[38] B. Davis and W. M. Stempel, Phys. Rev. **17**, 608 (1921).
[39] S. K. Allison and J. H. Williams, Phys. Rev. **35**, 1476 (1930).
[40] S. K. Allison, Phys. Rev. **41**, 1 (1932).
[41] C. G. Darwin, Philosophical Magazine Series 6 **27**, 315 (1914).
[42] C. G. Darwin, Philosophical Magazine Series 6 **27**, 675 (1914).
[43] J. A. Prins, Z. Phys. **63**, 477 (1930).
[44] B. Davis and H. Purks, Proceedings of the National Academy of Sciences **13**, 419 (1927).
[45] B. Davis and H. Purks, Proceedings of the National Academy of Sciences **14**, 172 (1928).
[46] S. K. Allison, Phys. Rev. **44**, 63 (1933).
[47] M. M. Schwarzschild, Phys. Rev. **32**, 162 (1928).
[48] A. H. Compton, Rev. Sci. Instrum. **2**, 365 (1931).
[49] J. H. Williams and S. K. Allison, J. Opt. Soc. Am. **18**, 473 (1929).
[50] J. H. Williams, Phys. Rev. **40**, 636 (1932).
[51] J. A. Bearden, Phys. Rev. **37**, 1210 (1931).
[52] J. A. Bearden, Phys. Rev. **38**, 2089 (1931).
[53] J. A. Bearden, Phys. Rev. **41**, 399 (1932).
[54] A. H. Compton and S. K. Allison, *X-rays in theory and Experiment*, 2nd ed. (D. Van Nostrand Company, Inc, Toronto New York London, 1935).
[55] R. W. James, *The optical principles of the Diffraction of X-rays*, The crystalline state, Vol. II (G. Bell and Sons, LTD, London, 1948).
[56] U. Bonse and M. Hart, Appl. Physics Letters **6**, 155 (1965).
[57] M. Hart, J. Phys. D: Appl. Phys. **1**, 1405 (1968).
[58] R. D. Deslattes and A. Henins, Phys. Rev. Lett. **31**, 972 (1973).
[59] P. Becker, K. Dorenwendt, G. Ebeling, R. Lauer, W. Lucas, R. Probst, H.-J. Rademacher, G. Reim, P. Seyfried, and H. Siegert, Phys. Rev. Lett. **46**, 1540 (1981).

[60] Y. Okada and Y. Tokumaru, J. Appl. Phys. **56**, 314 (1984).
[61] L. Ferroglio, G. Mana, and E. Massa, Optics Express **16**, 16877 (2008).
[62] E. Massa, G. Mana, and U. Kuetgens, Metrologia **46**, 249 (2009).
[63] E. Massa, G. Mana, U. Kuetgens, and L. Ferroglio, New Journal of Physics **11**, 053013 (2009).
[64] R. D. Deslattes, Rev. Sci. Instrum. **38**, 616 (1967).
[65] E. Kessler, J., R. D. Deslattes, and A. Henins, Phys. Rev. A **19**, 215 (1979).
[66] R. D. Deslattes, E. G. Kessler, W. C. Sauder, and A. Henins, Annals of Physics **129**, 378 (1980).
[67] J. Schweppe, R. D. Deslattes, T. Mooney, and C. J. Powell, Journal of Electron Spectroscopy and Related Phenomena **67**, 463 (1994).
[68] E. G. Kessler, R. D. Deslattes, D. Girard, W. Schwitz, L. Jacobs, and O. Renner, Phys. Rev. A **26**, 2696 (1982).
[69] R. Geller, in *Electron Cyclotron Resonance Ion Sources and ECR plasmas* (Institute of Physics, Bristol, 1996).
[70] C. Bieth, J. L. Bouly, J. C. Curdy, S. Kantas, P. Sortais, P. Sole, and J. L. Vieux-Rochaz, Rev. Sci. Instrum. **71**, 899 (2000).
[71] A. Gumberidze, D. Attia, C. I. Szabo, P. Indelicato, A. Vallette, and S. Carmo, Journal of Physics: Conference Series **163**, 012110 (2009).
[72] A. Gumberidze, M. Trassinelli, N. Adrouche, C. I. Szabo, P. Indelicato, F. Haranger, J.-M. Isac, E. Lamour, E.-O. L. Bigot, J. Merot, C. Prigent, J.-P. Rozet, and D. Vernhet, Rev. Sci. Instrum. **81**, 033303 (2010).
[73] R. Soria Orts, J. R. Crespo, L.-U., H. Bruhns, A. J. González Martínez, Z. Harman, U. D. Jentschura, C. H. Keitel, A. Lapierre, H. Tawara, I. I. Tupitsyn, J. Ullrich, and A. V. Volotka, Phys. Rev. A **76**, 052501 (2007).
[74] V. Mäckel, R. Klawitter, G. Brenner, J. R. Crespo López-Urrutia, and J. Ullrich, Phys. Rev. Lett. **107**, 143002 (2011).
[75] J. L. Campbell and T. Papp, At. Data. Nucl. Data Tab. **77**, 1 (2001).
[76] J. M. Paros and L. Weisbord, Machine Design , 151 (1965).
[77] R. D. Deslattes, J. Kessler, E. G., S. Owens, D. Black, and A. Henins, Journal of Physics D (Applied Physics) **32**, A3 (1999).
[78] E. G. Kessler, A. Henins, R. D. Deslattes, L. Nielsen, and M. Arif, J. Res. Natl. Inst. Stand. Technol. **99**, 1 (1994).
[79] J. Kessler, E. G., S. M. Owens, A. Henins, and R. D. Deslattes, IEEE Transactions on Instrumentation and Measurement **48**, 221 (1999).
[80] K. Fujii, A. Waseda, N. Kuramoto, S. Mizushima, P. Becker, H. Bettin, A. Nicolaus, U. Kuetgens, S. Valkiers, P. Taylor, D. B. Paul, G. Mana, E. Massa, R. Matyi, J. Kessler, E. G., and M. Hanke, IEEE Transactions on Instrumentation and Measurement **54**, 854 (2005).
[81] P. J. Mohr, B. N. Taylor, and D. B. Newell, Rev. Mod. Phys. **80**, 633 (2008).
[82] B. Andreas, Y. Azuma, G. Bartl, P. Becker, H. Bettin, M. Borys, I. Busch, M. Gray, P. Fuchs, K. Fujii, H. Fujimoto, E. Kessler, M. Krumrey, U. Kuetgens, N. Kuramoto, G. Mana, P. Manson, E. Massa, S. Mizushima, A. Nicolaus, A. Picard, A. Pramann, O. Rienitz, D. Schiel, S. Valkiers, and A. Waseda, Phys. Rev. Lett. **106**, 030801 (2011).
[83] E. Massa, G. Mana, L. Ferroglio, E. G. Kessler, D. Schiel, and S. Zakel, Metrologia **48**, S44 (2011).
[84] P. J. Mohr and B. N. Taylor, Rev. Mod. Phys. **77**, 1 (2005).
[85] CODATA, "Internationally recommended values of the fundamental physical constants 2010," (2011), http://physics.nist.gov/cuu/Constants/index.html.
[86] W. H. Zachariasen, *Theory of X-ray diffraction in crystals* (Dover Publications, New York, 1967).
[87] M. Sanchez del Rio and J. Dejus, in *SPIE proceedings* (1998) p. 3448.
[88] M. Sanchez del Rio and R. J. Dejus (SPIE, 2004) pp. 171–174.
[89] M. Sanchez del Rio and R. J. Dejus, AIP Conference Proceedings **705**, 784 (2004).
[90] S. Stepanov, "X0h on the web," .
[91] O. M. Lugovskaya and S. A. Stepanov, Soviet physics. Crystallography **36**, 478 (1991).
[92] W. H. Press, B. P. Flannery, S. A. Teukolsky, and W. T. Vetterling, *Numerical Recipes* (Cambridge University Press, Cambridge, 1986).
[93] B. L. Henke, E. M. Gullikson, and J. C. Davis, At. Data. Nucl. Data Tab. **54**, 181 (1993).
[94] D. Waasmaier and A. Kirfel, Acta Crystallographica Section A **51**, 416 (1995).
[95] C. T. Chantler, Journal of Physical and Chemical Reference Data **24**, 71 (1995).
[96] L. Kissel, Radiation Physics and Chemistry **59**, 185 (2000).
[97] C. T. Chantler, Journal of Physical and Chemical Reference Data **29**, 597 (2000).
[98] C. T. Chantler, "Detailed tabulation of atomic form factors, photoelectric absorption and scattering cross section, and mass attenuation coefficients for z = 1-92 from e = 1-10 ev to e = 0.4-1.0 mev," (2011).
[99] P. Amaro, *Study of forbidden transitions in atomic systems*, Ph.D. thesis, Universidade Nova de Lisboa (2011).
[100] B. H. Armstrong, Journal of Quantitative Spectroscopy and Radiative Transfer **7**, 61 (1967).
[101] H. Jian and Z. Qingguo, Journal of Optics A: Pure and Applied Optics **9**, 565 (2007).
[102] P. Indelicato, *Contribution à l'étude spectroscopique de transitions doublement excitées du fer heliumoïde*, Thèse de troisième cycle, Université Pierre et Marie Curie (1983).
[103] A. N. Artemyev, V. M. Shabaev, V. A. Yerokhin, G. Plunien, and G. Soff, Phys. Rev. A **71**, 062104 (2005).
[104] J. A. Bearden and J. S. Thomsen, J. Appl. Cryst. **4**, 130 (1971).
[105] T. Mooney, E. Lindroth, P. Indelicato, E. Kessler, and R. D. Deslattes, Phys. Rev. A **45**, 1531 (1992).
[106] S. Biri, A. Valek, T. Suta, E. Takacs, C. Szabo, L. T. Hudson, B. Radics, J. Imrek, B. Juhasz, and J. Palinkas, Rev. Sci. Instrum. **75**, 1420 (2004).
[107] S. Brennan and P. L. Cowan, Rev. Sci. Instrum. **63**, 850 (1992).
[108] G. G. Luther, R. D. Deslattes, and W. R. Towler, Review of Scientific instruments **55**, 747 (1984).
[109] L. Hudson, Private Communication (2000).